

How special are brightest group and cluster galaxies?

Anja von der Linden,^{1*} Philip N. Best,² Guinevere Kauffmann¹
and Simon D. M. White¹

¹Max Planck Institut für Astrophysik, Karl-Schwarzschild-Str. 1, Postfach 1317, 85741 Garching, Germany

²SUPA, Institute for Astronomy, Royal Observatory Edinburgh, Blackford Hill, Edinburgh EH9 3HJ

Accepted 2007 May 3. Received 2007 April 27; in original form 2006 November 7

ABSTRACT

We use the Sloan Digital Sky Survey (SDSS) to construct a sample of 625 brightest group and cluster galaxies (BCGs) together with control samples of non-BCGs matched in stellar mass, redshift and colour. We investigate how the systematic properties of BCGs depend on stellar mass and on their privileged location near the cluster centre. The groups and clusters that we study are drawn from the C4 catalogue of Miller et al. but we have developed improved algorithms for identifying the BCG and for measuring the cluster velocity dispersion. Since the SDSS photometric pipeline tends to underestimate the luminosities of large galaxies in dense environments, we have developed a correction for this effect which can be readily applied to the published catalogue data. We find that BCGs are larger and have higher velocity dispersions than non-BCGs of the same stellar mass, which implies that BCGs contain a larger fraction of dark matter. In contrast to non-BCGs, the dynamical mass-to-light ratio of BCGs does not vary as a function of galaxy luminosity. Hence BCGs lie on a different Fundamental Plane than ordinary elliptical galaxies. BCGs also follow a steeper Faber–Jackson relation than non-BCGs, as suggested by models in which BCGs assemble via dissipationless mergers along preferentially radial orbits. We find tentative evidence that this steepening is stronger in more massive clusters. BCGs have similar mean stellar ages and metallicities to non-BCGs of the same mass, but they have somewhat higher α/Fe ratios, indicating that star formation may have occurred over a shorter time-scale in the BCGs. Finally, we find that BCGs are more likely to host radio-loud active galactic nuclei than other galaxies of the same mass, but are less likely to host an optical active galactic nucleus (AGN). The differences we find are more pronounced for the less massive BCGs, i.e. they are stronger at the galaxy group level.

Key words: galaxies: clusters: general – galaxies: elliptical and lenticular, cD – galaxies: fundamental parameters.

1 INTRODUCTION

The central galaxies in galaxy clusters seem to be special – in many cases, the differences are visually obvious, because central cluster galaxies often have extended envelopes (i.e. they are cD galaxies) and they are usually the brightest (and most massive) galaxies in their clusters. The term *brightest cluster galaxy* (BCG) has thus become synonymous with the term *central galaxy*.

At first glance, it might seem evident that the location of the BCG at the bottom of the potential well of a cluster must be the cause for any property which distinguishes it from other (cluster) galaxies. However, BCGs are also the dominant population at the massive end of the galaxy luminosity function, and thus, their properties are influenced both by their large masses and by the cluster environment. It is very difficult to disentangle these two influences, because it is

difficult to find equally massive non-BCGs for comparison. Since most BCGs are early-type galaxies, their properties are often compared with the known scaling relations for elliptical galaxies. It has been claimed that BCGs lie on the same Fundamental Plane as other ellipticals (Oegerle & Hoessel 1991), but that they lie off its projections (e.g. the Faber–Jackson and Kormendy relations) in that they have lower velocity dispersions and larger radii than predicted by these relations (Thuan & Romanishin 1981; Hoessel, Oegerle & Schneider 1987; Schombert 1987; Oegerle & Hoessel 1991). More recently, it has been claimed that the slopes of the Faber–Jackson and Kormendy relations change as a function of galaxy luminosity for all elliptical galaxies (Desroches et al. 2007; Lauer et al. 2007). On the other hand, Brough et al. (2005) find that the surface brightness profiles (and thus the radii) of BCGs depend on the host cluster properties.

The formation mechanism of BCGs is also a subject of much debate. Early on, it was suggested that BCGs form when galaxies sink to the bottom of the potential well of a cluster and merge

*E-mail: anja@mpa-garching.mpg.de

(termed *galactic cannibalism*; Ostriker & Tremaine 1975; White 1976). However, Merritt (1985) argued that tidal stripping would reduce the masses of cluster galaxies to the point where dynamical friction is too slow for this to be a viable mechanism. These analyses assumed that clusters are *static entities*. A further mechanism to form BCGs *in situ* in the cluster is star formation in cluster *cooling flows*. At the centres of clusters, gas reaches high enough density to cool and condense into the cluster core (Silk 1976; Fabian 1994). However, while the mass deposition rates inferred from the X-ray luminosities of cooling flow clusters are of the order of several hundreds to $>1000 M_{\odot} \text{ yr}^{-1}$ (e.g. Allen et al. 1996), observed star formation rates are at most $\sim 100 M_{\odot} \text{ yr}^{-1}$ (Crawford et al. 1999). Recent X-ray studies have furthermore demonstrated that the cluster gas does not cool below $\sim 2 \text{ keV}$ (e.g. Peterson & Fabian 2006). Moreover, this scenario predicts that the stellar populations of BCGs should be young and blue, which is clearly inconsistent with observations.

These scenarios were proposed before hierarchical structure formation was fully established as the standard cosmological paradigm, and for simplicity they neglected many of the processes that take place when clusters assemble through mergers. Dubinski (1998) used *N*-body simulations to show that a dominant galaxy forms naturally by merging of massive galaxies when a cluster collapses along filaments. Recently, De Lucia & Blaizot (2007) investigated the formation of BCGs in the context of the Millenium Run simulation (Springel et al. 2005). In their model, the stars that make up BCGs today are formed in a number of galaxies at high redshifts, which subsequently merge to form larger systems. The final BCGs assemble rather late: by a redshift of $z \sim 0.5$, on average about half of the final stellar mass lies in the largest progenitor galaxy. Since many of these mergers take place very late when most galaxies have converted the bulk of their gas into stars, the merging events are very nearly dissipationless and are not associated with significant star formation. This scenario is supported by observations that demonstrate that BCGs exhibit little scatter in luminosity over a wide range of redshifts (Sandage 1972; Schneider, Gunn & Hoessel 1983; Postman & Lauer 1995; Aragon-Salamanca, Baugh & Kauffmann 1998), and that their colour evolution is consistent with a passively evolving stellar population that formed at high redshifts ($z_{\text{form}} \sim 2\text{--}5$).

Boylan-Kolchin, Ma & Quataert (2006) used two-component *N*-body simulations of galaxy mergers to show that the remnants of dissipationless mergers remain in the Fundamental Plane. They showed, however, that the locations of the remnants *within* the Fundamental Plane, and thus on projected relations such as the Faber–Jackson and size–luminosity relations, depend on the orbits of the merging galaxies. During cluster assembly, infall occurs primarily along filaments, suggesting that mergers on to the BCG may take place preferentially on radial orbits. Boylan-Kolchin et al. (2006) show that BCGs would then be predicted to lie on steeper Faber–Jackson and size–luminosity relations than field galaxies.

Although BCGs are probably not formed in cooling flows, they are believed to play an important role in regulating the rate at which gas cools at the centres of groups and clusters. The central cluster galaxies often harbour radio-loud active galactic nuclei (AGNs), which may provide the necessary heating to counteract radiative cooling. Burns (1990) finds that 10 out of 14 cD galaxies in cooling flow clusters are radio-loud, compared to three out of 13 in clusters without cooling cores. However, Best et al. (2005b) show that radio-loudness also depends strongly on other galaxy parameters such as stellar mass.

This work aims at comparing the properties of BCGs to those of ‘normal’ galaxies of similar stellar mass, thereby disentangling the influences of mass and environment. Our work is based on data from the Sloan Digital Sky Survey (SDSS; Section 2). It has recently been noted that the SDSS photometric pipeline tends to underestimate the luminosities of BCGs – we present a method to retrieve more accurate magnitudes from the catalogued data in Section 2 and Appendix A. To construct a sample of BCGs, we refine the C4 sample of galaxy clusters (Miller et al. 2005) in the SDSS by improving the selection of the central galaxy (Section 3). We also improve the C4 cluster velocity dispersion measurement by developing an iterative algorithm to simultaneously determine the redshift, the velocity dispersion and the virial radius of each cluster (Section 3). A detailed comparison of the measured BCG positions, redshifts and velocity dispersions to the original C4 values is given in Section 4. In Section 5 we investigate the occurrence of radio-loud AGN in BCGs. The results demonstrate that our choice of BCG is superior to the original choice of BCG in the C4 catalogue. The radio properties of the BCGs are investigated in more detail in an accompanying paper (Best et al. 2007), as are the implications of these results for models of cluster cooling flows. We compare BCGs to control samples of non-BCGs that are closely matched in stellar mass; we analyse their structural properties, their positions with respect to the Fundamental Plane and its projections, their stellar populations and their line emission in Section 6. A summary of our paper is given in Section 7.

Our refined BCG/cluster sample, together with the wealth of information available from the SDSS, also provides a local comparison sample for optically selected high-redshift clusters such as the ESO (European Southern Observatory) Distant Cluster Survey (White et al. 2005; EDiSCS). While this work focuses on the BCG selection and on properties of the BCGs, another paper (von der Linden et al., in preparation) will concentrate on cluster properties such as substructure, mass estimates from velocity dispersion as compared to total light, and the properties of cluster galaxies as a function of their distance from the BCG.

Unless otherwise noted, we assume a concordance cosmology with $\Omega_{\text{m}} = 0.3$, $\Omega_{\Lambda} = 0.7$ and $H_0 = 100 h \text{ km s}^{-1} \text{ Mpc}^{-1}$, where $h = 0.7$.

2 DATA

The SDSS (York et al. 2000; Stoughton et al. 2002) is a survey of about a quarter of the extragalactic sky, obtaining photometry in five bands (*ugriz*) of more than 200 million objects and spectra of up to a million objects. The observations are carried out in drift-scan mode on a dedicated 2.5-m telescope at Apache Point Observatory, with a large-array CCD camera that allows near-simultaneous photometry. The imaging data are reduced by an automatic pipeline, PHOTO (Lupton et al. 2001), and various classes of objects are then classified for subsequent spectroscopy; those galaxies with $14.5 < m_r < 17.7$ and $\mu < 24.5 \text{ mag arcsec}^{-2}$ comprise the ‘main galaxy sample’ (Strauss et al. 2002). The spectra are obtained using a fibre-fed spectrograph on the same telescope. On each spectroscopic plate, which has a circular field of view of radius $1:49$, 592 object fibres can be placed. Because of the finite fibre size, any two fibres on the same plate need to be spaced at least 55 arcsec apart. The fibre allocation is performed by a tiling algorithm, which maximizes the number of objects that can be observed (Blanton et al. 2003). In the case of a ‘fibre collision’ (i.e. two objects that are closer than 55 arcsec), no preference of objects is given within the usual constraints.

Our analysis is based on the Data Release 4 (DR4) of SDSS, whose main galaxy sample provides spectra for more than 500 000 galaxies.

2.1 Spectral analysis

A multitude of physical properties have been derived for galaxies in the spectroscopic data base via stellar population synthesis fitting and are publicly available.¹ The stellar continuum of each galaxy is modelled as a sum of template spectra generated from population synthesis models (Kauffmann et al. 2003a; Tremonti et al. 2004). These fits also lead to measures of the stellar mass-to-light ratio, star formation histories and mean stellar ages (Kauffmann et al. 2003a,b). After subtracting the stellar continuum, emission line fluxes can be accurately measured, allowing studies of the star formation rates (Brinchmann et al. 2004) and AGN activity (Kauffmann et al. 2003c; Heckman et al. 2004).

2.2 Photometry and stellar masses

It has recently been noted that the SDSS photometry systematically underestimates the luminosities of nearby BCGs (Bernardi et al. 2007; Lauer et al. 2007). The problem arises because the level of sky background is overestimated both for large objects and in crowded fields. This is not only a problem for BCGs, but also for all large galaxies, and the problem is worse in dense cluster environments. Since any estimate of the stellar mass of a galaxy is derived from its luminosity, it is crucial for our analysis to avoid biases in the luminosity measurement.

Apart from the local sky background measurement, which is estimated and applied for each galaxy, PHOTO provides a global sky measurement estimated over a whole field. In Appendix A, we argue that by adding up to 70 per cent of the difference between local and global sky to the radial surface brightness profiles (as provided by PHOTO), more accurate photometry can be achieved. We test this procedure using aperture photometry of 35 BCGs from the survey of Postman & Lauer (1995) that are contained in the area of sky covered by the SDSS Data Release 5 (DR5). We also test our corrected magnitudes by comparing with the photometry provided by Two Micron All Sky Survey (2MASS; Skrutskie et al. 2006). Our correction method (described in detail in Appendix A) has been applied to the BCGs as well as to about 200 000 unique galaxies at $z \lesssim 0.1$, which form the basis of our comparison samples for the BCGs.

Since many BCGs are observed to have surface brightness profiles which do not follow a simple de Vaucouleurs profile (Gonzalez, Zabludoff & Zaritsky 2005; Bernardi et al. 2007), we choose not to use a magnitude measurement that assumes a certain profile, or is sensitive to the profile shape (this includes Petrosian magnitudes, which include about 80 per cent of the light from galaxies with de Vaucouleurs brightness profiles, but almost 100 per cent of the light from galaxies with exponential light profiles). Instead, we measure isophotal magnitudes, defined as the light within the radius $r_{\text{iso}23}$ where the one-dimensional (1D) surface brightness profile reaches a surface brightness of $(23 + 10 \log(1 + z)) \text{ mag arcsec}^{-2}$ in the r band (the redshift term accounts for cosmological surface brightness dimming). This is a relatively bright isophote limit, chosen both to avoid residual uncertainties in the sky background subtraction (cf. Fig. A1) as well as to exclude light from the cD envelope present in some BCGs (which is noticeable typically at surface brightness

levels 1 or 2 mag fainter, cf. Gonzalez et al. 2005). We refer to these magnitudes as *iso23* magnitudes.

Other studies of BCGs have quantified their luminosities within metric apertures (e.g. Postman & Lauer 1995). These studies were focused on cD galaxies, whereas our study includes BCGs of a much broader range in mass and size. Hence metric apertures would include very different fractions of light for BCGs at the extreme ends of the mass range, cf. Fig. 3, and any result based on them would be very difficult to interpret. It can be argued that the *iso23* magnitudes are also dependent on the profile shape: for shallower brightness profiles, a larger fraction of the total light/mass is missed. However, an estimate of the total light is unfortunately not feasible due to residual uncertainties in the sky subtraction. We therefore adopt the *iso23* magnitudes as the least biased and least problematic luminosity measurements. However, we have verified that our (qualitative) results do not change if we use Petrosian magnitudes as an attempt to measure total magnitudes.

Stellar mass estimates for the BCGs and the comparison galaxies are derived from these luminosity measurements using the KCORRECT algorithm (Blanton & Roweis 2007), which is also used to determine the k -corrections for our galaxies. BCGs that were not observed spectroscopically (see Section 3.1) are assumed to have a redshift identical to the cluster redshift. Just as the luminosities should not be taken as an estimate of the total light, the quoted stellar masses are not an attempt to measure the total stellar mass. However, since our analysis is based on comparing objects with similar masses and colours, this is not an issue.

2.3 Radio catalogue

Best et al. (2005a) identified the radio-emitting galaxies within the main spectroscopic sample of the SDSS Data Release 2 (DR2), by cross-comparing these galaxies with a combination of the National Radio Astronomy Observatory (NRAO) Very Large Array (VLA) Sky Survey (NVSS; Condon et al. 1998) and the Faint Images of the Radio Sky at Twenty centimetres (FIRST) survey (Becker, White & Helfand 1995). They then used the optical properties of the galaxies to separate the radio-loud AGN from the radio-detected star-forming galaxies. This work has now been extended to include the DR3 (Data Release 3) and DR4 data (Best et al., in preparation), and these results were used to identify those galaxies that are radio-loud AGN.

3 SELECTION OF CLUSTERS AND BRIGHTEST CLUSTER GALAXIES

The basis of our cluster sample is the C4 cluster catalogue (Miller et al. 2005). The C4 catalogue is derived using the SDSS spectroscopic sample and is currently available for DR3. It identifies clusters in a parameter space of position, redshift and colour. The algorithm assumes that at least a fraction of the cluster galaxies form a colour–magnitude relation. It identifies galaxies in clustered regions, with neighbours of similar colours, as ‘C4 galaxies’ (see Miller et al. 2005, for a detailed discussion of this selection). From these C4 galaxies, it reconstructs the local density field, and identifies the C4 galaxies at the peaks of this density field as cluster centres (coined the *mean* galaxies).

The C4 catalogue identifies 1106 clusters within $0.02 \leq z \leq 0.16$. In order to ensure that our clusters span a large angular extent compared to the minimum distance between fibres (55 arcsec), we limit our cluster sample to $z \leq 0.1$. At this redshift, the magnitude limit of the spectroscopic sample corresponds to $M_r \sim -20$, i.e.

¹ <http://www.mpa-garching.mpg.de/SDSS/>

slightly fainter than an L^* galaxy. This cut results in a starting sample of 833 clusters.

3.1 Selection of the brightest cluster galaxy

Our aim is to find the galaxy closest to the deepest point of the potential well of the cluster. In many rich clusters, this choice is obvious, and the central galaxy can easily be recognized as a cD elliptical galaxy by its extended envelope. Typically, this is also the BCG. However, in some clusters the central, dominant galaxy may not be the brightest galaxy. An example is the cluster C4_2003,² shown in Fig. B1. The obvious central galaxy is SDSS J215729.42–074744.5 at the centre of the image, but it is 0.3 mag fainter than SDSS J215701.71–075022.5, about 6 arcmin west-south-west of the former. We identify the former as the BCG (but concede that the term is a misleading nomenclature in this case).

The C4 catalogue lists two galaxies for each cluster that could be considered the BCG: the *mean* galaxy (described above) and the brightest galaxy from the spectroscopic catalogue within $500 h^{-1}$ kpc of the position of the mean galaxy, four times the velocity dispersion and without strong H α emission. However, due to the problem of fibre collisions, the true BCG is not included in the SDSS spectroscopic data for about 30 per cent of the clusters and is thus missed by the C4 algorithm.

An earlier version of the C4 catalogue tried to correct for this by selecting a BCG based on the photometric catalogue. This object was selected to lie within $1 h^{-1}$ Mpc of the cluster centre, and have a colour compatible with the colour–magnitude relation of that cluster. Visual checks revealed, however, that this did not provide a reliable BCG: out of a subsample of 128 clusters, 17 of the photometric BCGs identified by C4 were stars misclassified as galaxies, and 36 were spiral galaxies (some of these located at the edge of the cluster).

To identify the BCG for each cluster, we use the following procedure.

(i) Based on the cluster redshift and velocity dispersion given by C4, we estimate the virial radius of the cluster:

$$R_{200} = 1.73 \frac{\sigma_{v,cl}}{1000 \text{ km s}^{-1}} \frac{1}{\sqrt{\Omega_{\Lambda} + \Omega_0(1 + z_{cl})^3}} h^{-1} \text{ Mpc} \quad (1)$$

(see Finn et al. 2005). As C4 lists velocity dispersions within fixed physical radii (0.5, 1, 1.5, 2, $2.5 h^{-1}$ Mpc), we use the minimum non-zero value of these different values in this step.

(ii) Within the projection of the larger of R_{200} and 0.5 Mpc around the *mean* galaxy, we select the two brightest galaxies that meet the following criteria.

- The concentration index $c = R_{90}/R_{50}$ is larger than 2.5 (where R_{90} is the radius containing 90 per cent of the Petrosian flux measured in the i band and R_{50} is the radius containing 50 per cent of this flux), and $\text{fracDeV}_i > 0.5$ (this is a measure of the contribution of the de Vaucouleurs profile to the SDSS model r magnitude). These cuts select galaxies likely to be early-types.

- The colour is compatible with that of the C4 *mean* galaxy to within $\Delta(u - g) \leq 0.6$ (unless one of the u magnitudes has a large error estimate), $\Delta(g - r) \leq 0.5$, $\Delta(r - i) \leq 0.4$ and $\Delta(r -$

- $i) \leq 0.4$ (these are the dimensions of the colour criteria originally used in the C4 algorithm to identify clustering in colour space).

- The flag TARGET_GALAXY has been set and the flag SATURATED is not set (these criteria allow us to identify stars that have been misclassified as galaxies, but they also apply to some low-redshift bright galaxies).

- If the object has spectroscopic data, we require that the redshift is within $\Delta z < 0.01$ from the cluster redshift.

The brightest galaxy that meets these criteria is our initial BCG candidate. However, it is possible that these criteria select a foreground elliptical. Thus, if the second brightest galaxy is more than 1 mag fainter than the brightest, we also consider it as a BCG candidate.

(iii) We then loosen some of these criteria:

- we require only $c > 2.3$;

- there is no constraint on $\Delta(u - g)$;

- TARGET_GALAXY does not need to be set, and SATURATED can be set.

Galaxies which meet this second set of criteria and are brighter than (both) the candidate(s) selected in the previous step enter the list of candidates. Unfortunately, misclassified stars enter our candidate lists at this stage.

(iv) (a) If this procedure returns only one candidate, which agrees with the spectroscopic BCG given by C4, then this is automatically considered the correct choice. This is the case for 242 clusters.

(b) If this is not the case, then the BCG candidates (those given by C4 and those identified by our criteria) are inspected visually. For this purpose, we examine 2.5×2.5 arcmin² colour images of the BCG candidates [provided by the DR4 Catalog Archive Server (CAS)³]. These thumbnail images allow us to

- identify cD galaxies by their extended envelope;
- identify stars misclassified as galaxies;
- identify obvious foreground ellipticals.

In the same step, a colour image of the cluster (encompassing a field slightly larger than R_{200}) can be viewed, with the BCG candidates marked. An impression can thus be gained of how the positions of the candidates relate to the C4 cluster centre(s) (as given by the *mean* galaxy and the geometric cluster centre, based on the mean of the positions of the C4 cluster galaxies), visible galaxy overdensities and other structures in the field. If there is more than one galaxy left in the candidate list, this colour image allows us to choose the (brightest) one at the centre of the galaxy overdensity identified by C4. In case such an overdensity is not apparent, we choose the brightest elliptical galaxy in the vicinity of the *mean* galaxy.

For 472 clusters, the BCG can be identified fairly easily by means of these thumbnail images and the cluster image.

(c) In case the previous step does not allow an unambiguous choice of the BCG, we enlarge the candidate list by adding galaxies within 2 Mpc that meet the criteria cited above. Along with this set of thumbnail images, we also inspect a colour image where galaxies within $\Delta z < 0.01$ from the cluster redshift and 2 Mpc from the *mean* galaxy have been marked (see Fig. B1). It is this image that allows us to visualize the clustering and to follow the galaxy distribution at the redshift in question. BCG candidates belonging to neighbouring clusters can be identified. Conversely, if the C4 cluster corresponds to a weak number density fluctuation

² A note on the cluster IDs: the IDs used in the DR3 version of C4 are not identical to those in the DR2 version. Since the DR3 catalogue was released only within the SDSS collaboration, the DR2 IDs are the ‘official’ IDs, so whenever possible, we identify clusters by their DR2 ID (e.g. C4_2003). For those clusters without a DR2 ID, we use the DR3 ID, and denote these as e.g. C4_DR3_2004.

³ <http://cas.sdss.org/astro/en/>

within another cluster, the BCG of this larger cluster is chosen. We identify the BCG of 54 clusters in this step.

(d) The remaining 65 clusters require further scrutiny. For some of these clusters, this is necessary because the galaxy we identify as the central, dominant galaxy is not contained in the list of candidates. In other cases, it is evident from the cluster images that the cluster is in fact part of a larger cluster. In this step, we use the Finding Chart, Navigate and Explore tools of the CAS website interactively. We start by marking galaxies within 2 Mpc and $\Delta z < 0.01$ from the *mean* galaxy (as before), but then altering the radius, centre and redshift range to gain an impression of the clustering. We identify the centre of the nearest galaxy overdensity and choose the most likely BCG within it. The colour and brightness criteria that were previously used to determine the BCG candidate(s) are not applied in this step.

At this stage, a given galaxy may have been identified as the BCG for more than one cluster. We then keep only the cluster whose *mean* galaxy is closest to the BCG. This rejects 101 clusters as being substructures of other clusters.

3.2 Determination of the velocity dispersion and the virial radius

The C4 algorithm measured velocity dispersions within fixed radii (see Section 4.3 for a more detailed discussion of the C4 velocity dispersions). We prefer to measure the velocity dispersion $\sigma_{v,cl}$ within the virial radius R_{200} , which can be related to the velocity dispersion and cluster redshift z_{cl} via equation (1). We thus developed an iterative algorithm to determine these three quantities.

(i) From the catalogue of galaxies described in Section 2.1, we select those that lie within $2 R_{start}$ from the BCG, where R_{start} is determined using equation (1) with $\sigma_{v,cl}$ given by the average value of the cluster velocity dispersions measured by C4. We also require the galaxies to lie within $\Delta z < 0.025$ of the cluster redshift.

(ii) For our first estimate of z_{cl} , we take the redshift given by C4, z_{cl}^{C4} . For the first estimate of $\sigma_{v,cl}$ (and R_{200}), we use the median absolute deviation of the starting sample of galaxies with respect to z_{cl}^{C4} . We also limit this first estimate to be less than 500 km s^{-1} , a step that is necessary to exclude surrounding large-scale structure.

(iii) For each galaxy, we calculate its velocity within the cluster rest frame:

$$\frac{v_i}{c} = \frac{z_i - z_{cl}}{1 + z_{cl}} \quad (2)$$

(iv) From those galaxies within $\pm 3\sigma_{v,cl}$ of z_{cl} , and within R_{200} from the BCG, we redetermine z_{cl} , $\sigma_{v,cl}$ (and thus also R_{200}) using the biweight estimator from Beers, Flynn & Gebhardt (1990).

(v) Steps (iii) and (iv) are repeated until convergence is reached, i.e. subsequent iterations differ by less than 0.1 per cent in z_{cl} and $\sigma_{v,cl}$. Galaxies are allowed to re-enter the sample. The galaxies contained in the final sample are considered the cluster galaxies.

It may happen that the iteration finds an oscillating solution, i.e. iteration $n + 2$ yields the same solution (and the same galaxies) as iteration n . In this case, the algorithm modifies the input $\sigma_{v,cl}$ to a random value between the two solutions and continues. Furthermore, the convergence criterion is relaxed by factor of 2 every 200 iterations. A maximum of 1000 iterations is allowed.

(vi) To estimate the error on the velocity dispersion, we draw 10 000 bootstrap realizations from the cluster galaxies and calculate

the velocity dispersion of each. We adopt 68 per cent confidence intervals as our estimate of the $\pm 1\sigma$ error.

For 55 clusters, the algorithm does not converge or its sigma- and radius-clipping subsequently remove all (or all but one) of the galaxies from the starting sample. Since these systems cannot be considered bound, they are removed from the cluster list.

At this point, all the clusters are inspected visually. We check a colour image of the cluster with the cluster galaxies marked, as well as the redshift histogram. We mark clusters with the following indications that either the choice of BCG or the definition of cluster membership may be improved.

- The redshift histogram does not justify the value of the velocity dispersion. For clusters in very rich environments, the velocity dispersion can be overestimated if galaxies of neighbouring groups and filaments are included. Clusters with a velocity dispersion exceeding 1500 km s^{-1} are automatically flagged, but also those with two or more spikes in the redshift histogram. 59 clusters are marked in this step.

- Some of the cluster images show that the selected BCG is not at the centre of the clustering. In others, there may be another bright elliptical present which could be the BCG, or the true BCG did not meet the criteria used to select BCG candidates (i.e. mostly late-type BCGs). 67 clusters are listed for re-investigation in this step.

- Clusters in which the BCG redshift (if in the spectroscopic data base) differs from the cluster redshift by more than $\Delta z = 0.002$ are also flagged (15 clusters).

In this second round of visual checking, the choice of BCG or the sigma- and radius-clipping limits can be changed. The former is done if the previously selected BCG is clearly associated with a substructure of a larger cluster, but also if there is a possibly better BCG candidate that was previously missed. Note that many of these alternative BCGs are in fact foreground objects – whenever possible, we retrieve redshift information on these objects from CAS or the NASA/IPAC Extragalactic Data base (NED).⁴ For 21 clusters, the ‘new’ BCG has not previously been selected as the BCG of another cluster. For 35 ‘clusters’, the BCG has been attributed to another cluster, and so these systems are considered infall regions of these other clusters and discarded from the list. The sigma- and radius-clipping limits are changed for 53 clusters to avoid galaxies in nearby structures being included as cluster members (the sigma clipping is typically changed from 3σ to 2.5σ or 2.0σ – note that this affects only the choice of galaxies from which $\sigma_{v,cl}$ and z_{cl} are determined; cluster membership is still defined to be within $3\sigma_{v,cl}$ and R_{200}). For 67 clusters, nothing is changed.

At this stage, we discard those systems that only contain two or three galaxies within $3\sigma_{v,cl}$ and $1R_{200}$. This leaves 625 entries in our cluster sample. Fig. 1 shows a histogram of the number of spectroscopic members for our cluster sample. The original C4 catalogue considered only clusters with at least eight galaxies within $1 h^{-1} \text{ Mpc}$ and $\Delta z = 0.02$. This is a much larger volume than we probe, and it is thus not surprising that we typically assign fewer galaxies to each cluster.

Our final cluster sample spans a large range in velocity dispersion, from groups of $\lesssim 200 \text{ km s}^{-1}$ to clusters of over 1000 km s^{-1} (Fig. 2). The positions of our BCGs as well as the cluster properties determined by our algorithm are listed in Table 1. Those systems with velocity dispersions $\lesssim 300\text{--}400 \text{ km s}^{-1}$ are more likely to be galaxy

⁴ <http://nedwww.ipac.caltech.edu/>

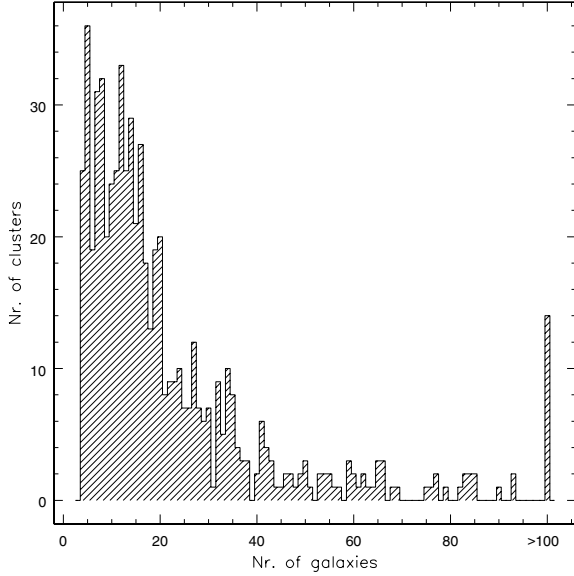


Figure 1. Histogram of the number of spectroscopic members within $\pm 3\sigma_{v,cl}$ and $1R_{200}$ for our final cluster sample. Those clusters with ≥ 100 members are grouped into a single bin. The cluster with the most members is C4_DR3_3031 (Abell 2199) with 263 members.

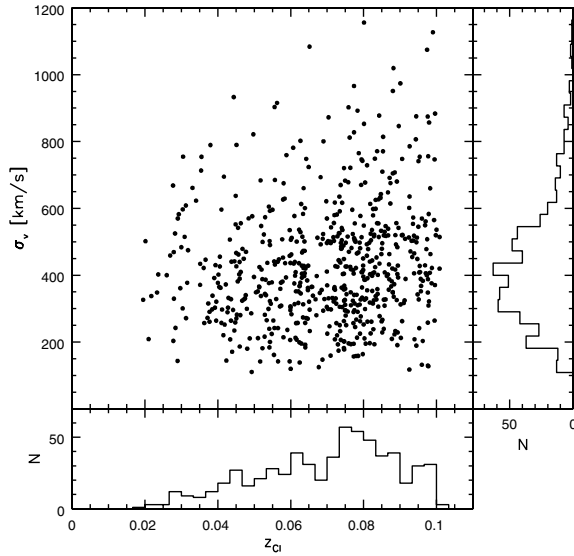


Figure 2. Distribution of the redshifts and velocity dispersions we measure for our final cluster sample. Error bars have been omitted for clarity. The marginal histograms show the distribution binned in redshift (lower panel) and in velocity dispersion (right-hand panel).

groups than galaxy clusters. We use the terms ‘cluster’ and ‘brightest cluster galaxy’ loosely in this paper to refer to both clusters and groups.

Fig. 3 presents a gallery of BCGs, sorted according to the velocity dispersion of the parent cluster (every 18th BCG is shown). The appearance of the BCG is certainly a function of $\sigma_{v,cl}$, but it is not a monotonic one. While the BCGs of groups are mostly fairly isolated, rather spherical elliptical galaxies, the BCGs of more massive systems are in general larger and more elongated, they often have a cD envelope and are surrounded by many satellite galaxies.

Table 1. Excerpt of our catalogue of BCGs for the C4 cluster catalogue, along with the cluster properties derived by our algorithm. The complete catalogue is available as Supplementary Material to the online article. Note that columns (1) and (2) refer to the C4 cluster ID (see footnote in Section 3.1); column (7) gives the number of galaxies from which the cluster redshift and velocity dispersion were determined.

ID_2 (1)	ID_3 (2)	α_{BCG} ($^{\circ}$) (3)	δ_{BCG} ($^{\circ}$) (4)	z_{cl} (5)	σ_v (km s $^{-1}$) (6)	N_{gal} (7)
1000	1000	202.5430	-2.1050	0.087	648 $^{81}_{-90}$	35
1001	1001	208.2767	5.1497	0.079	746 $^{57}_{-59}$	82
1002	1002	159.7776	5.2098	0.069	800 $^{57}_{-56}$	90
1003	1004	184.4214	3.6558	0.077	966 $^{58}_{-60}$	127
1004	1005	149.7174	1.0592	0.081	458 $^{48}_{-52}$	21
1005	1006	191.3037	1.8048	0.048	340 $^{53}_{-55}$	24
1007	1009	177.4721	5.7008	0.075	404 $^{40}_{-43}$	27
1009	1011	198.0566	-0.9745	0.085	631 $^{71}_{-75}$	36
1010	1012	192.0112	-1.6528	0.088	420 $^{77}_{-80}$	14
1011	1013	227.1073	-0.2663	0.091	748 $^{61}_{-66}$	42
-	1014	220.1785	3.4654	0.027	459 $^{34}_{-35}$	105
1013	1015	203.0701	1.2233	0.079	327 $^{59}_{-74}$	10
1014	1016	175.2992	5.7348	0.098	660 $^{54}_{-56}$	55
1015	1017	182.5701	5.3860	0.077	596 $^{53}_{-59}$	41
1016	1018	154.9344	-0.6384	0.093	455 $^{137}_{-153}$	17
1017	1019	227.8480	-0.0593	0.091	509 $^{59}_{-64}$	36
1018	1020	214.3980	2.0532	0.054	605 $^{51}_{-53}$	69
1019	1021	195.7262	3.3174	0.071	496 $^{56}_{-59}$	24
-	1024	199.8197	-0.9954	0.083	579 $^{87}_{-91}$	37
1023	1025	153.4095	-0.9254	0.045	790 $^{52}_{-57}$	66
1341	1026	155.6325	2.3608	0.072	580 $^{71}_{-76}$	26
-	1027	191.9269	-0.1373	0.088	1020 $^{87}_{-91}$	55
1027	1028	199.1357	0.8702	0.080	364 $^{54}_{-60}$	16
1030	1030	206.1357	2.9541	0.077	511 $^{66}_{-73}$	29
-	1032	218.4964	3.7780	0.029	570 $^{58}_{-60}$	76
1032	1033	211.4731	-1.2045	0.054	184 $^{47}_{-64}$	4
-	1034	165.7398	7.6039	0.072	321 $^{41}_{-44}$	20
1034	1036	192.3087	-1.6874	0.085	771 $^{63}_{-67}$	64
1036	1038	151.8861	0.5942	0.097	550 $^{61}_{-65}$	29
-	1039	186.8781	8.8246	0.090	846 $^{63}_{-66}$	50
1037	1040	213.6360	1.7316	0.054	299 $^{37}_{-39}$	16
1038	1041	179.3707	5.0891	0.076	678 $^{66}_{-69}$	62
1039	1042	228.8088	4.3862	0.098	857 $^{86}_{-87}$	53
1040	1043	168.3339	2.5467	0.074	403 $^{56}_{-65}$	30
1041	1044	194.6729	-1.7615	0.084	771 $^{78}_{-81}$	60
1044	1047	197.3295	-1.6225	0.083	521 $^{84}_{-89}$	22
1045	1048	205.5402	2.2272	0.077	828 $^{77}_{-80}$	75
-	1050	206.1075	2.1099	0.072	514 $^{84}_{-92}$	14
1176	1051	189.7348	6.1584	0.074	486 $^{74}_{-82}$	19
1048	1053	147.9551	1.1339	0.063	346 $^{36}_{-39}$	13
1049	1054	188.7581	1.7986	0.079	577 $^{61}_{-65}$	35
1051	1057	177.8878	5.1015	0.075	251 $^{22}_{-25}$	11
1052	1058	195.7191	-2.5164	0.083	749 $^{62}_{-65}$	68
-	1059	156.4666	1.1906	0.097	478 $^{127}_{-154}$	12

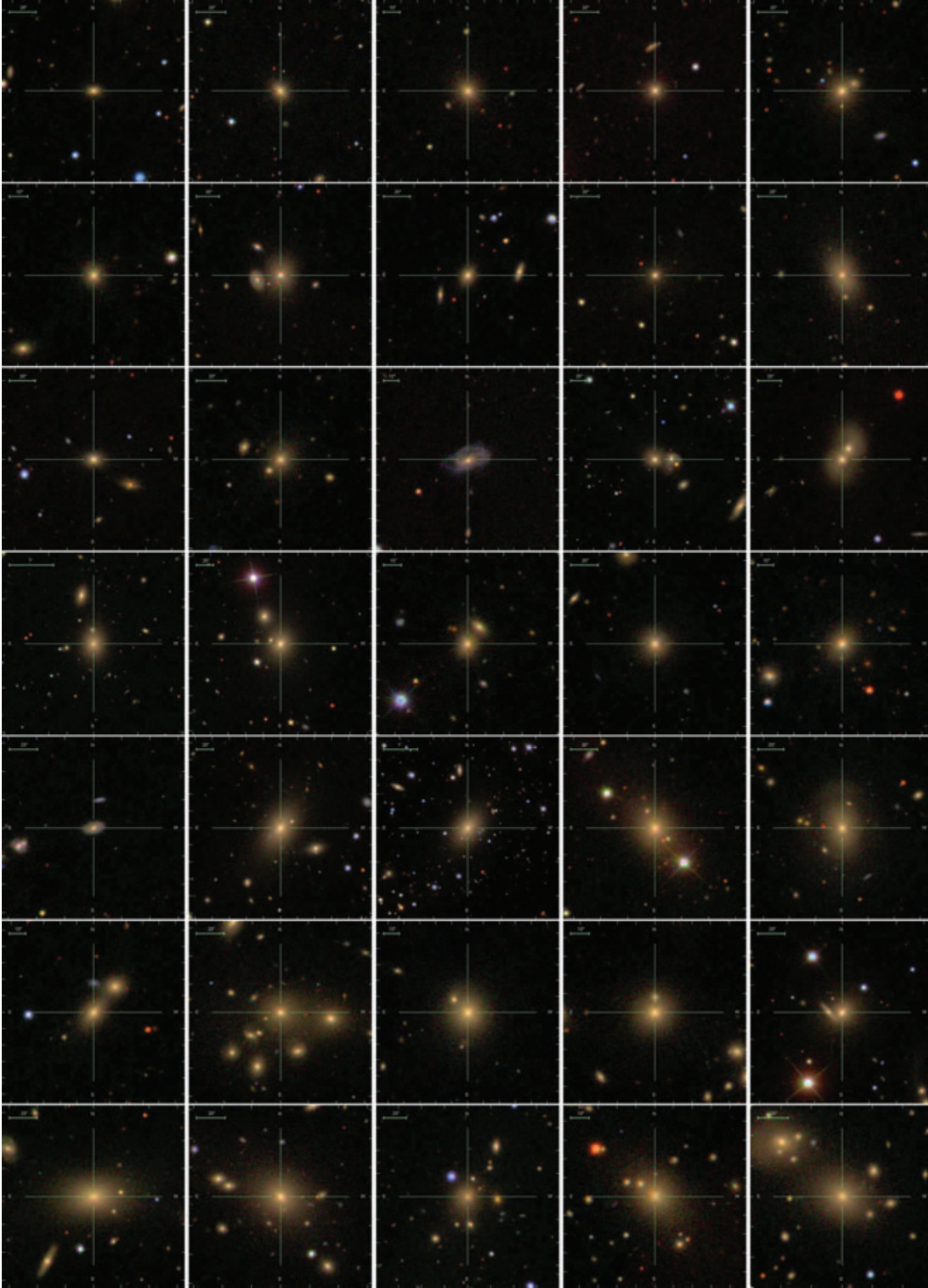


Figure 3. A gallery of BCGs. Each image is 200 kpc on the side. From left to right, top to bottom: C4_DR3_3351 ($\sigma_{v,cl} = 159 \text{ km s}^{-1}$), C4_2042 ($\sigma_{v,cl} = 195 \text{ km s}^{-1}$), C4_DR3_1343 ($\sigma_{v,cl} = 210 \text{ km s}^{-1}$), C4_3275 ($\sigma_{v,cl} = 233 \text{ km s}^{-1}$), C4_3087 ($\sigma_{v,cl} = 256 \text{ km s}^{-1}$), C4_DR3_3201 ($\sigma_{v,cl} = 264 \text{ km s}^{-1}$), C4_DR3_3106 ($\sigma_{v,cl} = 283 \text{ km s}^{-1}$), C4_1224 ($\sigma_{v,cl} = 299 \text{ km s}^{-1}$), C4_3206 ($\sigma_{v,cl} = 312 \text{ km s}^{-1}$), C4_2065 ($\sigma_{v,cl} = 324 \text{ km s}^{-1}$), C4_DR3_3272 ($\sigma_{v,cl} = 329 \text{ km s}^{-1}$), C4_DR3_1366 ($\sigma_{v,cl} = 342 \text{ km s}^{-1}$), C4_DR3_2140 ($\sigma_{v,cl} = 355 \text{ km s}^{-1}$), C4_3059 ($\sigma_{v,cl} = 365 \text{ km s}^{-1}$), C4_DR3_3386 ($\sigma_{v,cl} = 378 \text{ km s}^{-1}$), C4_DR3_1355 ($\sigma_{v,cl} = 392 \text{ km s}^{-1}$), C4_3068 ($\sigma_{v,cl} = 403 \text{ km s}^{-1}$), C4_DR3_3034 ($\sigma_{v,cl} = 410 \text{ km s}^{-1}$), C4_1025 ($\sigma_{v,cl} = 425 \text{ km s}^{-1}$), C4_1226 ($\sigma_{v,cl} = 435 \text{ km s}^{-1}$), C4_DR3_1360 ($\sigma_{v,cl} = 448 \text{ km s}^{-1}$), C4_3055 ($\sigma_{v,cl} = 467 \text{ km s}^{-1}$), C4_DR3_1356 ($\sigma_{v,cl} = 484 \text{ km s}^{-1}$), C4_1024 ($\sigma_{v,cl} = 500 \text{ km s}^{-1}$), C4_1076 ($\sigma_{v,cl} = 509 \text{ km s}^{-1}$), C4_1191 ($\sigma_{v,cl} = 519 \text{ km s}^{-1}$), C4_1073 ($\sigma_{v,cl} = 536 \text{ km s}^{-1}$), C4_DR3_3105 ($\sigma_{v,cl} = 556 \text{ km s}^{-1}$), C4_3009 ($\sigma_{v,cl} = 583 \text{ km s}^{-1}$), C4_DR3_1275 ($\sigma_{v,cl} = 617 \text{ km s}^{-1}$), C4_DR3_3027 ($\sigma_{v,cl} = 670 \text{ km s}^{-1}$), C4_1058 ($\sigma_{v,cl} = 721 \text{ km s}^{-1}$), C4_DR3_3084 ($\sigma_{v,cl} = 781 \text{ km s}^{-1}$), C4_DR3_3349 ($\sigma_{v,cl} = 884 \text{ km s}^{-1}$), C4_3002 ($\sigma_{v,cl} = 1156 \text{ km s}^{-1}$).

4 COMPARISON TO C4

4.1 Selected BCGs

For 31 clusters in the final sample, the BCG we identified corresponds to both the C4 *mean* galaxy and the spectroscopic BCG identified by C4. 19 of these were classified automatically, as there was no other candidate in our list.

In 343 clusters, our BCG is the same as the C4 spectroscopic BCG, but not the mean galaxy (183 automatically classified).

In 41 cases, the BCG is the same as the C4 *mean* galaxy, but not the C4 spectroscopic BCG. These are predominantly small systems, where the C4 spectroscopic BCG belongs to another system.

The BCGs of 210 clusters correspond neither to the *mean* galaxy nor to the C4 spectroscopic BCG. Of these, 141 (i.e. 23 per cent of the whole sample) are not in the spectroscopic catalogue.

In Fig. 4, we compare the positions of our BCGs with those of the C4 *mean* galaxies. For the majority of the clusters, these two positions fall within 500 kpc of one another. 53 BCGs lie farther than $500 h^{-1}$ kpc from the *mean* galaxy⁵ and of these, 21 lie farther away than 1 Mpc. At these distances, the original cluster centre is well in the outskirts of the structures we identify.

An example is C4_DR3_1283 (see Fig. B2), where the BCG and the original *mean* galaxy are separated by 2.8 Mpc, equivalent to $1.6 R_{200}$ according to the velocity dispersion we measure. The mean galaxy is a $10^{10} M_{\odot}$, star-forming galaxy at $z = 0.099$, in a rich field that is likely to be an infall region of the cluster. The BCG we identified (a $4 \times 10^{11} M_{\odot}$ elongated elliptical with a cD envelope) is at the centre of a cluster of 22 other galaxies. It is curious that this cluster was not picked up by the C4 algorithm. The comparatively high redshift of the cluster ($z = 0.095$) may possibly play a role in this. The cases of the other clusters with large separations between the BCG we identify and the C4 *mean* galaxy are similar, though less striking.

4.2 Cluster redshift measurements

The original C4 algorithm measures the cluster redshift using the biweight estimator of Beers et al. (1990) applied to all spectroscopic members within an aperture of $1 h^{-1}$ Mpc from the luminosity-weighted geometrical centre of the cluster and within $\Delta z = 0.02$ of the peak of the redshift histogram defined by these galaxies. While $1 h^{-1}$ Mpc is comparable to R_{200} for a cluster with a velocity dispersion of $\sim 600 \text{ km s}^{-1}$, the corresponding redshift interval from which we determine the redshift of such a cluster would be only $\Delta z = 0.006 (1 + z_{c,cl})$.

In Fig. 5, we plot the relative differences between the two redshift measurements as a function of the velocity dispersion $\sigma_{v,cl}^{C4}$ measured by C4 within $1 h^{-1}$ Mpc. Our new redshift lies outside the $1\sigma_{v,cl}^{C4}$ redshift interval for only a few clusters, and only one lies outside the $3\sigma_{v,cl}^{C4}$ limit. The most notable outlier is C4_DR3_2163, with a velocity offset of about 2400 km s^{-1} . In our cluster sample, C4_DR3_2163 is a group of four galaxies at a redshift of $z_{cl} = 0.070$ and a velocity dispersion of $225_{-101}^{+73} \text{ km s}^{-1}$. Its redshift histogram shows another spike of galaxies at a redshift of 0.082 which can be associated with C4_2124 (see Figs B3 and B4). We thus conclude that the C4 algorithm considered these two structures as a single cluster, whereas our algorithm was able to separate them.

⁵ $500 h^{-1}$ kpc is the radius within which the C4 algorithm identifies its spectroscopic BCG.

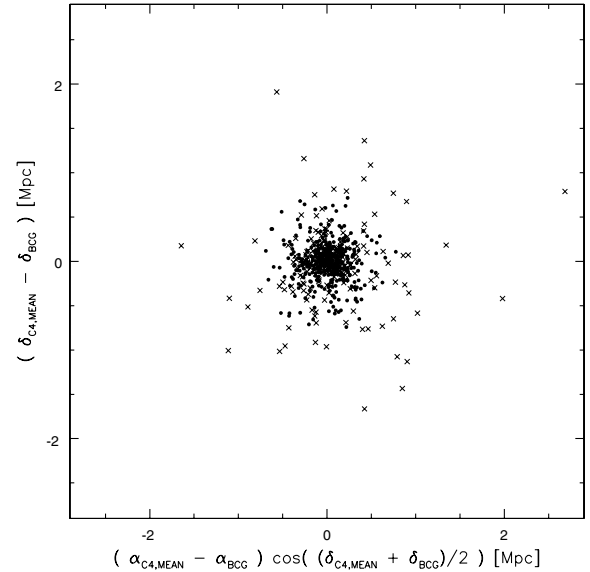


Figure 4. The differences in the positions of the C4 mean galaxy and our BCG, expressed in Mpc. Clusters in which the BCG is neither the mean galaxy nor the C4 spectroscopic BCG are shown as crosses, the other clusters are shown as filled circles.

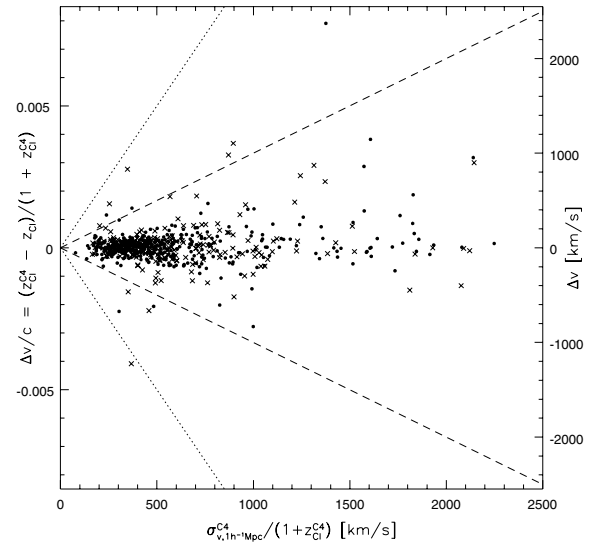


Figure 5. The differences between the C4 and our cluster redshift measurement (expressed as relative velocity) compared to the velocity dispersion $\sigma_{v,cl}^{C4}$ measured by C4 within $1 h^{-1}$ Mpc (expressed in the cluster rest frame). The dashed line indicates $\sigma_{v,cl}^{C4}$ and the dotted line $3\sigma_{v,cl}^{C4}$. As in Fig. 4, clusters in which the BCG is neither the *mean* galaxy nor the C4 spectroscopic BCG are shown as crosses, and as filled circles otherwise.

4.3 Velocity dispersion measurements

The C4 catalogue provides five measures of a cluster's velocity dispersion, measured within 0.5, 1, 1.5, 2 and $2.5 h^{-1}$ Mpc from the positional centroid measured on the sky. A first estimate for the velocity dispersion is made using the biweight estimator for all galaxies within $\Delta z = 0.02$ of the estimated cluster redshift. The final velocity dispersion (expressed in the observer's frame) is recomputed from galaxies within the redshift interval equal to $\pm 4\sigma_{v,cl}^{C4}$.

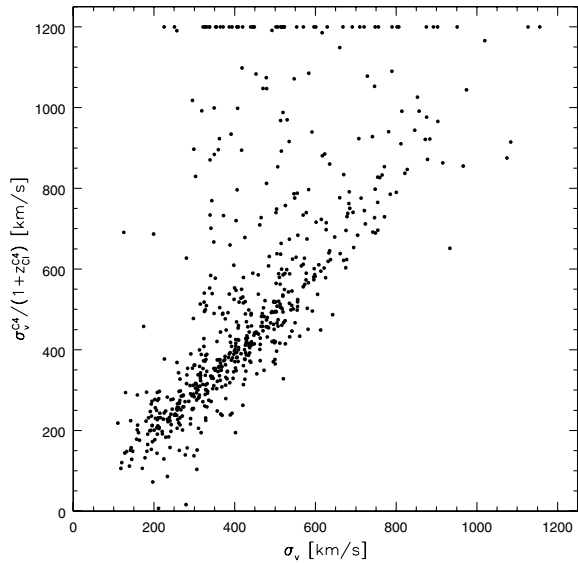


Figure 6. Comparison of the cluster velocity dispersions measured by C4 and by our algorithm. We adopt the C4 velocity dispersion measured within the radius that best corresponds to the virial radius measured from our algorithm. Those C4 values that are larger than 1200 km s^{-1} are plotted at this value.

Fig. 6 shows a comparison of our velocity dispersions to the C4 velocity dispersion within the radius that best corresponds to our estimate of the virial radius. At low velocity dispersions ($\sigma_{v,cl} \lesssim 600 \text{ km s}^{-1}$), the measurements agree well for many clusters. At higher velocity dispersions (as measured by C4) our algorithm obtains lower values for the majority of the clusters. As was previously shown for C4_DR3_2163, this is mainly caused by the fact that our iterative algorithm separates neighbouring groups/clusters better than C4.

5 RADIO-LOUD AGN ACTIVITY OF BCGs

It is known that BCGs often host radio-loud AGNs (e.g. Burns 1990). It has previously not been investigated whether this is simply a consequence of the strong dependence of radio-AGN activity on galaxy stellar mass ($f_{\text{radio-loud}} \propto M_*^{2.5}$; Best et al. 2005b), or whether this is a special property of BCGs. With our large sample of BCGs, it is possible to disentangle the mass dependence and the influence of the cluster environment. Fig. 7 compares the fraction of galaxies that are radio-loud for the BCG sample with the results found for all SDSS galaxies that overlap the NVSS and FIRST surveys. BCGs of all luminosities/masses are more likely to be radio-loud than other galaxies of the same luminosity/stellar mass. This enhancement ranges from a factor of 10 at masses of $5 \times 10^{10} M_\odot$ to less than a factor of 2 above $4 \times 10^{11} M_\odot$. Best et al. (2005b) have argued that radio-AGN activity is fuelled from the hot gas envelopes of galaxies. In this scenario, groups and clusters provide an additional hot gas reservoir, which boosts the radio-AGN activity of the central galaxies. This result, and its implications for the cooling flow model, is investigated in more detail in the accompanying paper (Best et al. 2007).

In this paper, we use the enhanced radio-AGN fraction of BCGs as a diagnostic for the *reliability* of the BCG selection, i.e. are our BCGs indeed better tracers of the bottom of the clusters' potential wells than the original C4 BCGs? In Fig. 8, we repeat the previous analysis for C4 BCGs. At the highest mass bins ($> 10^{11.1} M_\odot$), the C4 BCGs have a similar radio-loud fraction to our BCGs, but at lower masses, the radio-loud fraction is lower than in ours. We also investigate the radio-loud fraction in clusters where our method and the C4 algorithm select different BCGs (252 clusters). Here, the difference becomes even clearer: our BCGs have a much higher radio-loud fraction than those identified by C4.

In Fig. 9 we repeat this analysis on the C4 *mean* galaxies. A similar trend as for the C4 BCGs is seen.

These results can easily be explained by the difference in selection algorithm: in a cluster where the BCG is the most massive and

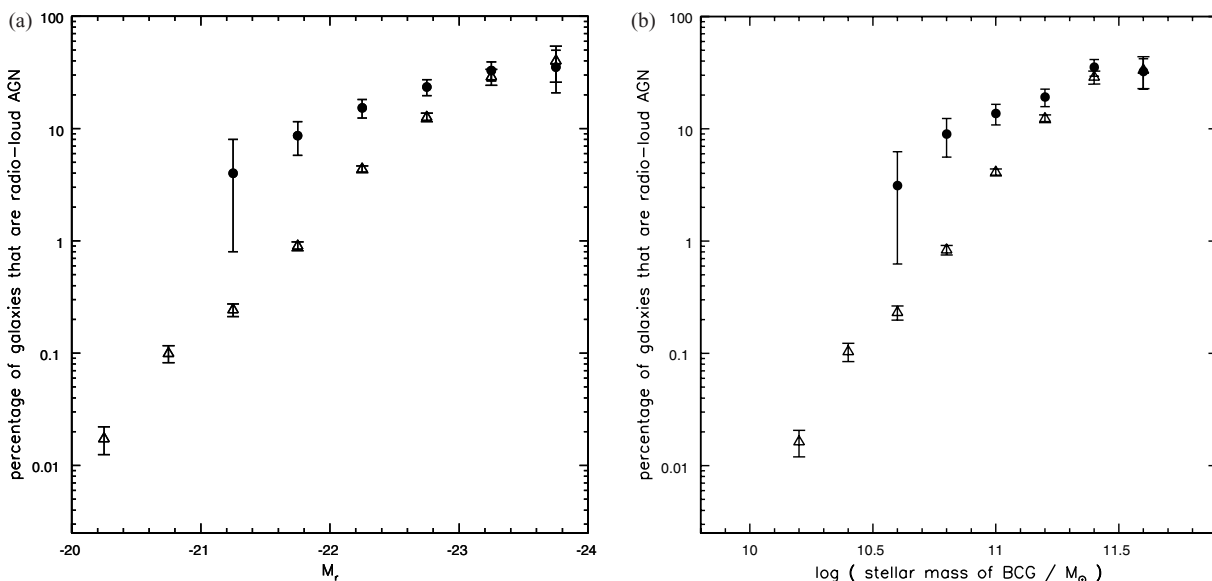


Figure 7. The fraction of galaxies that are radio-loud AGN, as a function of luminosity (left) and stellar mass (right). Results are plotted for all galaxies at $z < 0.1$ (open triangles), and for the BCGs (solid circles). Galaxies are considered radio-loud if their 1.4-GHz radio luminosity is greater than $10^{23} \text{ W Hz}^{-1}$, and they are not classified as star forming.

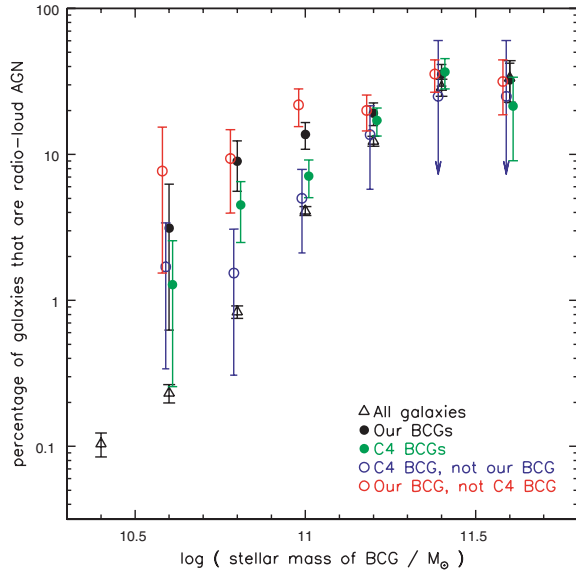


Figure 8. The radio-loud fraction of BCGs identified by C4 (green, filled circles), compared to those identified by our method (black, filled circles). We also show the radio-loud fractions derived only from clusters where the two choices differ: C4 BCGs are shown as blue, open circles; our BCGs are shown as red, open circles. Arrows indicate that the result is an upper limit only. The points are slightly offset in mass for clarity.

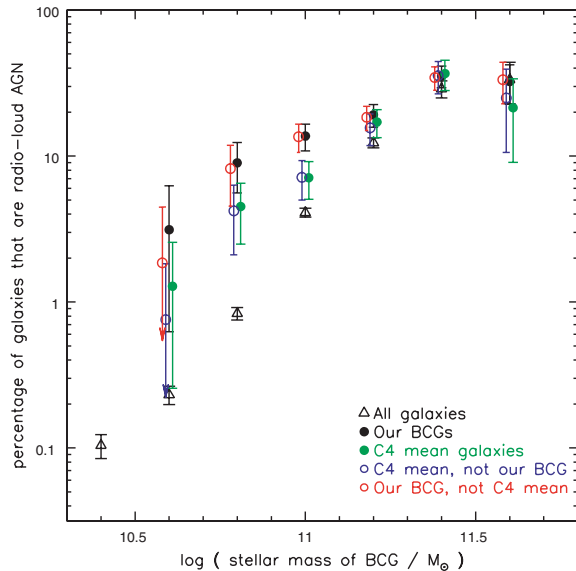


Figure 9. The same as Fig. 8, but for the C4 mean galaxies.

brightest galaxy and has spectroscopic information available, C4 will correctly identify it, and hence the agreement is good in the high mass bins. However, if C4 misses the ‘real’ BCG, for example due to fibre collisions, it classifies a less massive galaxy (typically not at the bottom of the potential well) as a BCG. Since these galaxies are normal cluster galaxies, their radio-loud fraction is lower than that of BCGs of equal mass. Hence, the C4 algorithm results in an underestimate of the radio-loud fraction at low masses.

6 OPTICAL PROPERTIES OF BCGS

Our large sample of BCGs and the extensive SDSS data base allow us to compare the structural properties of BCGs with those of

non-BCGs in order to distinguish the roles of mass and environment in governing their properties. In order to perform the comparison, we construct a comparison sample of ‘control’ galaxies for each BCG by finding its three closest neighbours in a space spanned (by the logarithm) of galaxy stellar mass, redshift and $g - r$ colour. The ‘redshift axis’ of this space is scaled by a factor of 5, so that a difference of 0.1 in $\log M_*$ corresponds to a redshift difference of 0.02, and a difference of 0.1 in $g - r$. The matching is performed in order of decreasing BCG mass, and galaxies are not allowed to enter the comparison sample more than once.

By matching in redshift, redshift-dependent aperture effects are avoided. The matching in $g - r$ ensures similar stellar populations and mass-to-light ratios in the BCGs and their controls, i.e. effectively, early-type BCGs are matched to early-type galaxies. Without the $g - r$ matching, there are more late-type galaxies in the control sample than the BCG sample. However, since our method of selecting BCGs is somewhat biased towards selecting early-type galaxies over late-types, we cannot unambiguously deduce that BCGs are more likely to be early-types.

The pool of galaxies from which the control sample is drawn consists of all galaxies in the DR4 spectroscopic catalogue that have not been identified as a BCG in our sample. Yet, at the very massive end ($\log M_*/M_\odot > 11.5$) there are not enough non-BCGs to provide three control galaxies per BCG. On the other hand, since we draw comparison galaxies from the full DR4 data base, whereas the C4 catalogue is based on DR3, the control sample is ‘contaminated’ by BCGs that failed to enter our sample, particularly for the most massive galaxies.⁶ Hence, for a large part of the analysis, we restrict the sample to BCGs with $\log M_*/M_\odot < 11.3$; this avoids the problem of finding three suitable non-BCGs for the comparison sample, and also purifies the comparison sample since at very high masses, a significant fraction of the comparison galaxies may themselves be BCGs. With these criteria, we construct two comparison samples, one for the full set of BCGs, and the other for the subset of BCGs with spectroscopic information.

In order to study scaling relations over a larger range in mass, we construct two more comparison samples (one drawn from all BCGs and one of them for BCGs with SDSS spectroscopy) with only one matched galaxy. Restricting to one comparison galaxy per BCG minimizes the problem of lack of comparison galaxies at the high-mass end. For this matching, we restrict our analysis to only early-type BCGs and comparison galaxies by requiring $M_g - M_r > 0.75$ and $\text{fracDeV}_r > 0.8$.

Our four comparison samples are summarized below.

CS3p: a comparison sample of three matching galaxies for BCGs with $\log M_*/M_\odot < 11.3$. The galaxies are matched in mass, redshift and $g - r$ colour.

CS3s: like CS3p, but for BCGs contained in the spectroscopic data base.

CS1p: a comparison sample of one matching galaxy for each BCG (with no upper mass limit). The sample is matched in mass, redshift and $g - r$ colour, and restricted to only

⁶ We have also attempted to clean the matched sample by applying the algorithm described in Section 3.2 to these galaxies, and considering those which are the brightest in structures of more than four galaxies to be possible BCGs. About one third of the matched galaxies are such BCG candidates. Basing our analysis on the remaining BCGs and the respective matched galaxies does not qualitatively alter our results.

early-type BCGs and comparison galaxies ($M_g - M_r > 0.75$ and $\text{fracDeV}_r > 0.8$).

CS1s: like CS1p, but for BCGs contained in the spectroscopic data base.

The first two samples are used to compare the *distributions* of physical parameters for BCGs and non-BCGs. The latter two samples are used to analyse early-type galaxy scaling relations, and to probe them to the highest masses.

In Figs 10 and 11 we present the distributions of a variety of photometric and spectroscopic parameters for the BCGs and the comparison samples CS3p and CS3s (characteristics of the distributions, i.e. the 16, 50 and 84 percentiles, are listed in Tables 2 and 3). For each parameter, we list the decimal logarithm of 1 minus the Kolmogorov–Smirnov confidence level at which the null hypothesis that the distributions are drawn from identical parent populations is rejected (i.e. a 99 per cent probability that the distributions are different will have a value of -2).

By construction, the BCGs and the comparison sample are identical in stellar mass, redshift and colour. Because both stellar mass and colour are the same, the distributions of luminosity are also equivalent.

Note that our stellar masses are calculated using the `KCORRECT` algorithm applied to isophotal magnitudes that have been corrected for sky-subtraction errors. These masses are not the same as the stellar masses estimated using the methods described in Kauffmann et al. (2003a), which we compare in Fig. 11(c). For the latter, the mass-to-light ratio determined from the continuum spectrum is applied to the SDSS Petrosian magnitude. Since these magnitudes underestimate the luminosity, the galaxy mass is underestimated as well. We also find that non-BCGs show stronger gradients between their fibre colours and their iso23 aperture colours (Fig. 10, cf. Section 6.3). Colour gradients imply that the mass-to-light ratio varies across the galaxy and this is not accounted for when deriving stellar masses from the spectra.

6.1 Structural parameters

6.1.1 Radii and surface brightness

In agreement with previous studies, we find that BCGs are larger (Figs 10f and g) and have lower surface brightnesses than non-BCGs (Figs 10h and i). The difference is more prominent for the inner characteristic radius R_{50} (defined as the radius containing half the galaxy’s light measured within the $r = 23 \text{ mag arcsec}^{-2}$ isophote) than for the outer isophotal radius $R_{\text{iso}23}$, within which we measure the luminosity of the galaxy. This is also evident in the distributions of the concentration parameter $c' = R_{\text{iso}23}/R_{50}$: for a given $R_{\text{iso}23}$, a BCG has a larger R_{50} than a non-BCG. This indicates that the light profiles of BCGs are systematically different to those of non-BCGs. To first order, these differences can be explained by BCGs having shallower light profiles. Indeed, Gonzalez et al. (2005) and Bernardi et al. (2007) find comparatively large Sersic indices (and thus shallow profiles) when fitting BCG light profiles with Sersic profiles.

6.1.2 Size–luminosity relation

The sizes and luminosities of elliptical galaxies have been shown to obey the scaling $R_{50} \propto L^\alpha$, with $\alpha \simeq 0.6$ (e.g. Bernardi et al. 2003b). However, at the massive end, this relation steepens (Lauer et al. 2006). Bernardi et al. (2007) argue that BCGs have larger

radii and that this steepening is caused by an increasing fraction of BCGs. Desroches et al. (2007) still find a steepening after removing the C4 BCGs from their sample of SDSS elliptical galaxies and argue that the steepening is not solely attributable to ‘contamination’ from a population of galaxies with intrinsically larger radii (BCGs).

The top right-hand panel of Fig. 12 *demonstrates* that BCGs are larger than non-BCGs at all luminosities or stellar masses. Symmetric linear fits to the individual data points yield very similar exponents for the radius–luminosity relation for the BCG sample and the comparison sample:

$$R_{50, \text{BCGs}} \propto L^{0.65 \pm 0.02},$$

$$R_{50, \text{CS1s}} \propto L^{0.63 \pm 0.02}.$$

However, we also find that the relation displays curvature, i.e. it steepens with luminosity. This is shown in the lower right-hand panel of Fig. 12. The range of exponents we find ($\alpha \sim 0.5\text{--}0.7$) is broadly consistent with that of Desroches et al. (2007). We note that α is only slightly larger for the BCGs than the non-BCGs, even at the highest luminosities. We do not find the significantly steeper relations claimed by Bernardi et al. (2007, $\alpha = 0.92$) and Lauer et al. (2007, $\alpha = 1.18$). Both of these samples include both BCGs and non-BCGs – the Bernardi et al. (2007) study uses the original C4 BCGs, which we have shown to be contaminated by non-BCGs, and the Lauer et al. (2007) study is based on galaxies with $M_V < -21$ and detectable core radii. Such contamination from non-BCGs is likely to be most important at lower luminosities, and will thus mimic a steeper slope. Even if we take this effect into account, our data do not support very large values of α ; if we fit a relation to the BCGs at $M_r \sim -23.5$ and non-BCGs at $M_r \sim -23$, we find a value of α of only 0.93. We speculate that one possible source for the discrepancy could be the different definitions of R_{50} used in the different studies.

6.1.3 Ellipticity

We calculate the axial ratios of the galaxies in our sample (Fig. 10k) from the flux-weighted second moments as measured by `PHOTO`, i.e.

$$b/a = \frac{1 - \sqrt{Q^2 + U^2}}{1 + \sqrt{Q^2 + U^2}}, \quad (3)$$

where Q and U are the Stokes parameters listed in the `PHOTO` data base. We choose this measurement since it is not based on fitting a particular model to the surface brightness profile of the galaxy and it is also not as sensitive to the sky subtraction as isophotal ellipticity measures. The majority of BCGs and non-BCGs are round, with axis ratios $b/a \gtrsim 0.8$. Both samples exhibit a tail to lower axial ratios, but this tail is more prominent for the non-BCGs. The median axial ratio is very similar for both samples (0.90 for the BCGs and 0.88 for the non-BCGs). This is qualitatively consistent with the results of Ryden, Lauer & Postman (1993). It should be noted, however, that Porter, Schneider & Hoessel (1991) find that the ellipticity of BCGs increases as a function of the radius at which it is measured (see also Gonzalez et al. 2005).

6.2 Dynamical structure

6.2.1 Velocity dispersion

As in previous studies of elliptical galaxies that used spectra taken within fixed-sized apertures (Jørgensen, Franx & Kjaergaard 1995;

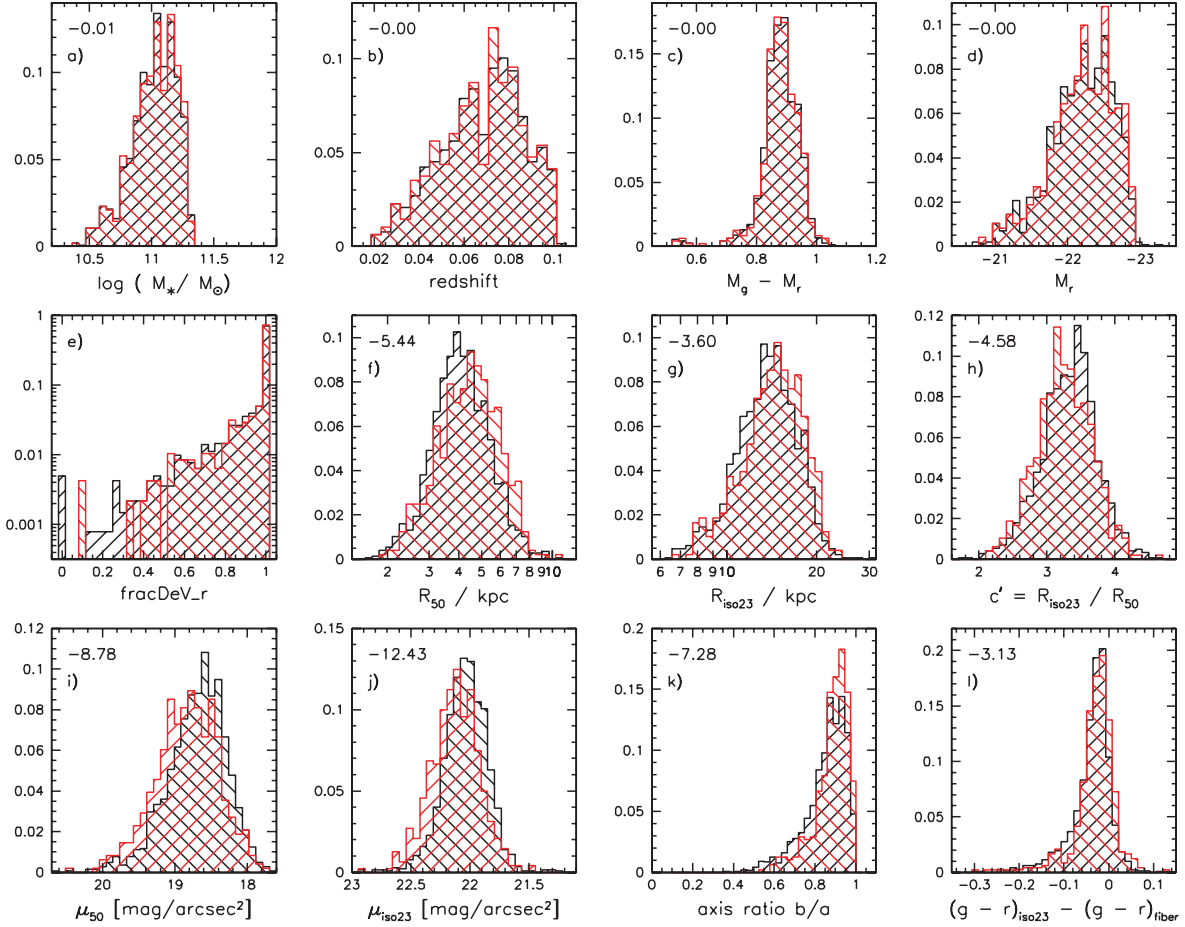


Figure 10. Distributions of a variety of photometric parameters for the sample of BCGs (red histograms) and the comparison sample, matched in stellar mass, redshift and $g - r$ (black histograms). The ordinate of each plot shows the fraction of galaxies in a particular bin. In the top left-hand corner of each panel we list the logarithm of the Kolmogorov–Smirnov probability that the two distributions are drawn from an identical parent population. From left to right, top to bottom, the panels show: stellar mass; redshift; $M_g - M_r$; M_r ; fracDeV_r ; the inner characteristic radius R_{50} , defined as the radius enclosing half the light measured within the isophotal radius $R_{\text{iso}23}$; the $r = 23 \text{ mag arcsec}^{-2}$ isophote radius $R_{\text{iso}23}$ (within which our magnitudes are defined); concentration parameter $c' = R_{\text{iso}23}/R_{50}$; average surface brightness μ_{50} within R_{50} ; the average surface brightness $\mu_{\text{iso}23}$ within $R_{\text{iso}23}$; axis ratio (from the flux-weighted second moments measured by PHOTO) and the colour gradient between the iso23 and the fibre apertures.

Table 2. The 16, 50 and 84 per cent percentiles (left, middle and right columns, respectively) of the distributions presented in Fig. 10. The values for the matched sample are listed in the top rows, those for the BCGs in the bottom rows.

$\log(M_*/M_\odot)$			z			$M_g - M_r$			M_r		
10.84	11.04	11.19	0.05	0.07	0.09	0.83	0.88	0.94	-22.62	-22.24	-21.76
10.84	11.04	11.20	0.05	0.07	0.09	0.84	0.88	0.94	-22.63	-22.24	-21.77
fracDeV_r			R_{50}/kpc			$R_{\text{iso}23}/\text{kpc}$			c'		
0.86	1.00	1.00	3.14	4.08	5.41	10.76	13.79	17.20	2.92	3.34	3.69
0.89	1.00	1.00	3.24	4.49	5.89	11.14	14.47	17.96	2.84	3.23	3.65
μ_{50}			$\mu_{\text{iso}23}$			b/a			$(g-r)_{\text{iso}23} - (g-r)_{\text{fibre}}$		
18.31	18.65	19.09	21.86	22.04	22.21	0.76	0.88	0.95	-0.07	-0.03	-0.00
18.41	18.82	19.26	21.93	22.12	22.32	0.81	0.90	0.96	-0.06	-0.02	0.00

Bernardi et al. 2003a), we correct the galaxy velocity dispersion to its expected value at one-eighth of the effective radius:

$$\sigma_v = \sigma_{v,\text{meas}} \left(\frac{r_{\text{fibre}}}{r_{50}/8} \right)^{0.04}, \quad (4)$$

where $\sigma_{v,\text{meas}}$ is the measured velocity dispersion, r_{fibre} is the radius of the SDSS fibre (1.5 arcsec) and r_{50} is the inner characteristic radius, measured in arcseconds. Strictly speaking, since the iso23 magnitudes do not attempt to measure the total galaxy light, r_{50} is not exactly the same as the effective radius, but because the

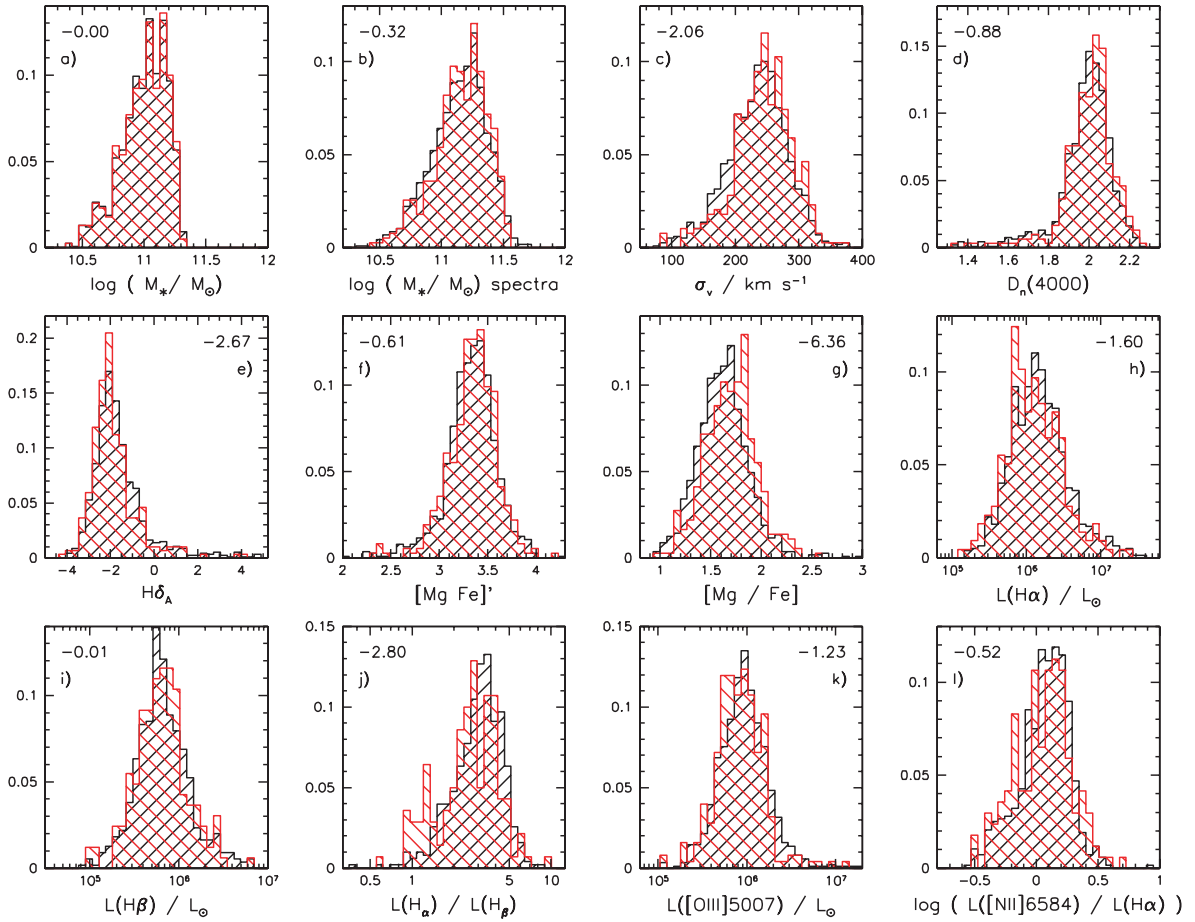


Figure 11. Same as Fig. 10, but for a comparison sample matched to the BCGs in the spectroscopic data base; showing the distributions of various (mainly) spectroscopic parameters. The first panel demonstrates the match in stellar mass. The other panels show: stellar mass as extrapolated from the mass-to-light ratio derived from the continuum spectrum; velocity dispersion; strength of the 4000-Å break; $H\delta_A$ index; the metallicity index $[Mg/Fe]'$; the alpha-to-iron index $Mgb/(Fe)$; $H\alpha$ line luminosity; $H\beta$ line luminosity; the Balmer decrement $H\alpha/H\beta$; the $[O\ III]5007$ line luminosity and the line ratio $[N\ II]/H\alpha$ (a projection of the BPT diagram).

Table 3. The 16, 50 and 84 per cent percentiles (left, middle and right columns, respectively) of the distributions presented in Fig. 11. The values for the matched sample are listed in the top rows, those for the BCGs in the bottom rows.

$\log(M_*/M_\odot)$			$\log(M_*/M_\odot)_{\text{spectra}}$			$\sigma/\text{km s}^{-1}$			$D_n(4000)$		
10.82	11.03	11.18	10.91	11.17	11.36	187	239	279	1.89	2.00	2.09
10.82	11.03	11.19	10.92	11.17	11.37	203	246	288	1.91	2.02	2.10
$H\delta_A$			$[Mg/Fe]'$			$Mgb/(Fe)$			$\log(L_{H\alpha}/L_\odot)$		
-2.57	-1.88	-0.80	3.11	3.35	3.56	1.38	1.62	1.85	5.81	6.14	6.53
-2.72	-2.07	-1.09	3.10	3.37	3.58	1.45	1.70	1.93	5.75	6.07	6.47
$\log(L_{H\beta}/L_\odot)$			$L_{H\alpha}/L_{H\beta}$			$\log(L_{[OIII]5007}/L_\odot)$			$L_{[NII]6584}/L_{H\alpha}$		
5.55	5.80	6.09	1.96	3.11	4.32	5.70	5.96	6.22	0.13	0.09	0.25
5.53	5.81	6.07	1.34	2.67	3.94	5.69	5.92	6.17	-0.19	0.07	0.26

correction does not scale very steeply with radius, this difference is negligible. This correction also assumes a universal velocity dispersion profile. While this seems to be applicable to most elliptical galaxies (Jørgensen et al. 1995), it has not yet been demonstrated that it also applies to BCGs.

We find that BCGs have systematically larger velocity dispersions than non-BCGs (Fig. 11c; this also holds for the uncorrected velocity dispersions).

6.2.2 Dynamical mass

The larger radii and higher velocity dispersions of BCGs imply that they have larger dynamical-to-stellar mass ratios than non-BCGs. The dynamical mass within R_{50} can be derived via a projection of the scalar virial theorem on to observable quantities:

$$M_{\text{dyn},50} = c_2 \frac{\sigma_v^2 R_{50}}{G}, \quad (5)$$

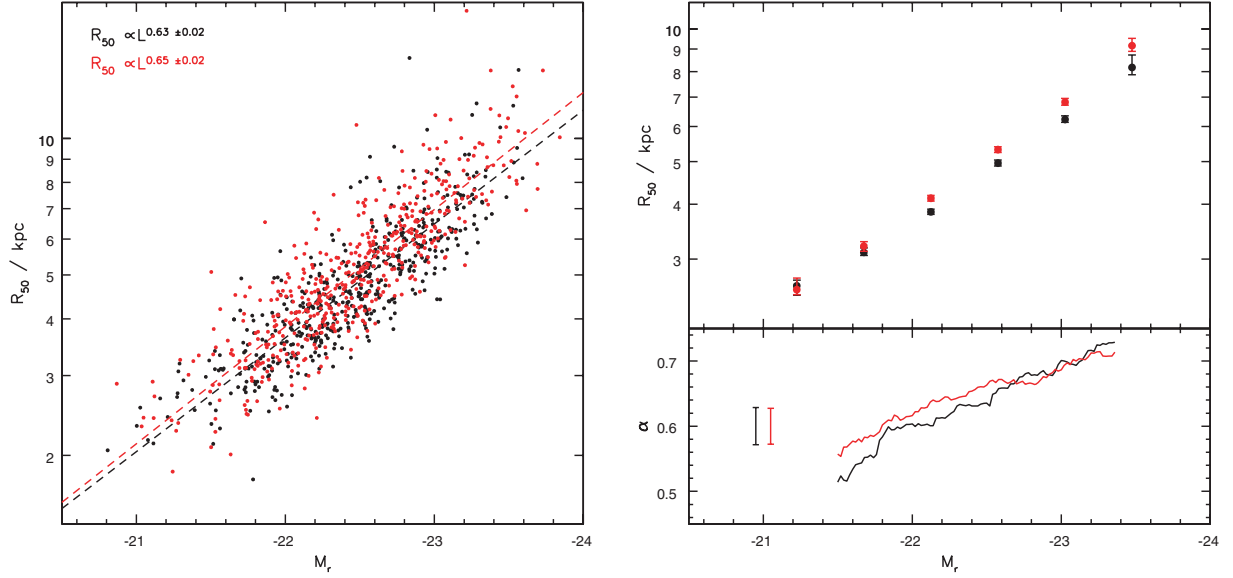


Figure 12. Left-hand panel: the size–luminosity relation for the BCGs (red) and for the comparison sample CS1p (black) along with the best-fitting linear relations (dashed lines). Top right-hand panel: the median radii in bins of magnitude. The error bars represent the 68 per cent confidence levels divided by the square root of the number of galaxies in the respective bin. Lower left-hand panel: the variation of α , the exponent of the size–luminosity relation, as a function of magnitude M_r , determined from galaxies within $M_r \pm 1.0$.

where c_2 depends on the profiles of both the dark matter and the luminous matter components. If the former follows an NFW profile (Navarro, Frenk & White 1997), and the latter a Hernquist (1990) profile, then $c_2 = (1.65)^2$ (Padmanabhan et al. 2004). For calculating the dynamical mass, we assume that $c_2 = (1.65)^2$:

$$M'_{\text{dyn},50} = M_{\text{dyn},50} \frac{(1.65)^2}{c_2} = (1.65)^2 \frac{\sigma_v^2 R_{50}}{G}. \quad (6)$$

We also assume that the stellar mass within R_{50} is 50 per cent of the stellar mass within $R_{\text{iso}23}$ (Padmanabhan et al. 2004). We find that the ratio of dynamical mass to stellar mass is indeed considerably larger for BCGs (Fig. 13). This difference is likely the consequence of the position of BCGs at or near the centres of galaxy clusters. As a result, there is a greater contribution from the dark matter halo to the dynamical mass of the BCG.

6.2.3 The Fundamental Plane

Early-type galaxies seem to be well described by a two-parameter set of equations, as is evidenced by the Fundamental Plane: they lie on a plane in a coordinate system defined by the logarithmic values of velocity dispersion σ_v , effective radius and average surface brightness within the effective radius (Djorgovski & Davis 1987). The plane is typically expressed as

$$R_e \propto \sigma_v^a I_e^{-b}. \quad (7)$$

While there is agreement that $b \simeq 0.8$, the parameter a is dependent on filter bands and may also be sensitive to a variety of selection effects and the precise definitions of σ_v , R_e and I_e . Typical values of $a \sim 1.2$ – 1.6 are quoted in the literature (see for example the compilation of observed FP coefficients in Bernardi et al. 2003c).

We assume that $b = 0.8$ and plot $\log(R_{50} I_{50}^{0.8})$ as a function of $\log \sigma_v$ in Fig. 14 for the early-type BCGs and the comparison sample CS1s. In this diagram, the BCGs and the comparison galaxies only diverge for galaxies with small radii and/or high surface brightness (i.e. these are not the cD galaxies). The difference is in the sense that the velocity dispersions of the BCGs are larger. A linear fit

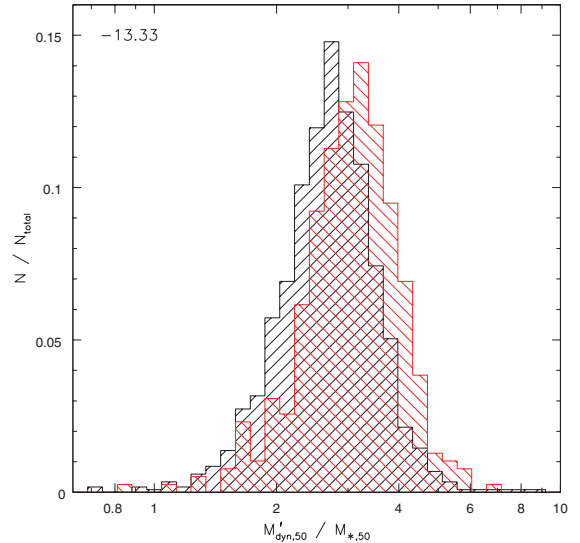


Figure 13. The ratio of dynamical mass to stellar mass (within R_{50}) for the BCGs (red) and the comparison sample CS3s (black). We have assumed that $c_2 = (1.65)^2$.

accounting for errors in both coordinates (FITEXY from Press et al. 1992) yields

$$a_{\text{BCGs}} = 1.96 \pm 0.10,$$

$$a_{\text{CS1s}} = 1.61 \pm 0.07.$$

For the comparison sample, the value of a lies close to the values that have been measured in the near-infrared (e.g. Pahre, Djorgovski & de Carvalho 1998, $a = 1.53 \pm 0.08$), and also in the SDSS (Bernardi et al. 2003c, $a = 1.49 \pm 0.05$). For the BCGs, a is significantly larger, indicating that BCGs do not lie on the same Fundamental Plane as ‘normal’ ellipticals. It is interesting to note that it is predominantly the small, low velocity dispersion BCGs which deviate from the generic Fundamental Plane.

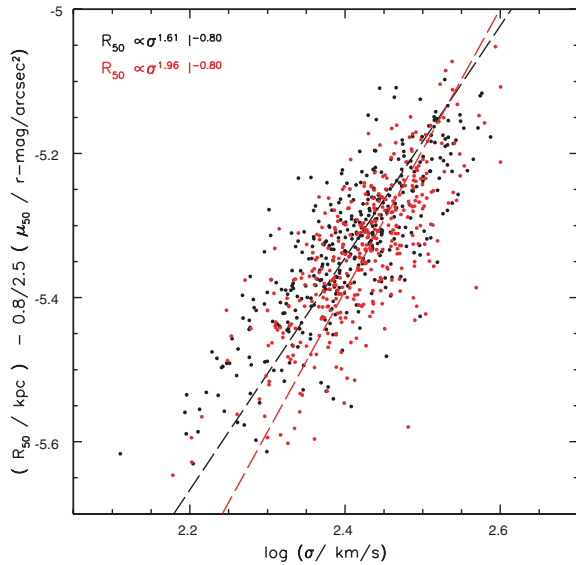


Figure 14. Projection along the Fundamental Plane BCGs (red) and the galaxies of CS1s (black). The dashed lines show the respective best fit for a , keeping $b = 0.8$.

The Fundamental Plane relation is essentially an expression of the virial theorem. If we write

$$M_* = c_1 L \quad \text{and} \quad L = 2\pi I_{50} R_{50}^2, \quad (8)$$

equation (5) can be rewritten as

$$R_{50} = \frac{1}{2\pi G} \frac{c_2}{c_1} \frac{M_*}{M_{\text{dyn},50}} \sigma_v^2 I_{50}^{-1}. \quad (9)$$

The deviation of the observed Fundamental Plane from the theoretical one ($a = 2$ and $b = 1$) is referred to as the ‘tilt’ of the Fundamental Plane. The tilt implies that $(c_2/c_1) (M_*/M_{\text{dyn},50})$ varies for different elliptical galaxies. The proportionality constant c_1 is an expression of the stellar mass-to-light ratio and varies for different stellar populations. c_2 depends on the profile shapes of both the luminous and the dark matter components. If c_2 were constant, elliptical galaxies would be structurally homologous systems. There are contradictory results in the literature as to whether it is predominantly non-homology or variation in $L/M_{\text{dyn},50}$ that is responsible for the tilt of the Fundamental Plane.

We are unable to distinguish non-homology from variation of $L/M_{\text{dyn},50}$ with our data. When calculating dynamical mass, we assume $c_2 = (1.65)^2$ (equation 6), but we caution that this approach necessarily neglects effects from non-homology.

In Fig. 15, we investigate how the pre-factor $(c_2/c_1)(M_*/M_{\text{dyn},50}) = (L/(M_{\text{dyn},50}/c_2))$ varies as a function of stellar mass for BCGs compared to non-BCGs. The results show that the variation is much smaller for the BCGs. This is an affirmation of our previous result that BCGs lie on a different Fundamental Plane than non-BCGs. It also demonstrates that this result does not come from a few outliers, but applies to the majority of galaxies with $M_* < 10^{11.3} M_\odot$. Since $(L/(M_{\text{dyn},50}/c_2))$ varies so little, the BCG Fundamental Plane is closer to the expectations of the virial theorem ($a = 2$ and $b = 1$).

Again, it is for low-mass galaxies that BCGs differ most from non-BCGs. The similarity between BCGs and non-BCGs at high stellar masses implies that the process(es) which cause this ratio to be approximately constant for BCGs also apply to massive non-BCGs. Possibilities include assembly history (e.g. the influ-

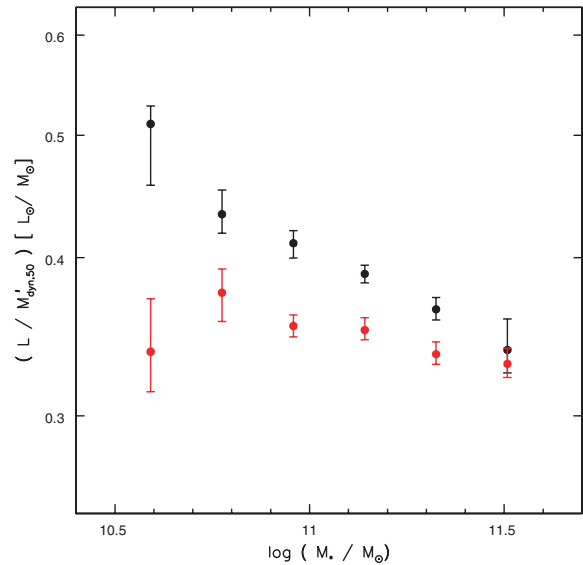


Figure 15. The median luminosity to dynamical mass ratio of BCGs (red) and the comparison sample CS1s (black) in bins of galaxy stellar mass. It is the variation of this ratio which determines the tilt of the Fundamental Plane.

ence of the orbital elements during dissipationless mergers; Boylan-Kolchin et al. 2006), and the fact that both BCGs and massive galaxies in general are found in dense environments (Kauffmann et al. 2004).

6.2.4 Faber–Jackson relation

Several studies suggest that BCGs follow a different relation between luminosity and velocity dispersion than less massive elliptical galaxies (Oegerle & Hoessel 1991; Bernardi et al. 2007; Lauer et al. 2007). Parametrizing this relation as $L \propto \sigma^\beta$, the canonical value is $\beta = 4$, as can be seen from equations (8) and (9), assuming that $(c_2/c_1) (M_*/M_{\text{dyn},50}) (1/I_{50})$ is constant. Most measurements reported in the literature are consistent with $\beta \simeq 4$ (e.g. Bernardi et al. 2003b). However, for samples of BCGs (Oegerle & Hoessel 1991) and very massive galaxies (Lauer et al. 2007), it is found that $\beta > 4$, i.e. σ increases less steeply with luminosity than predicted by the standard Faber–Jackson relation.

In Fig. 16, we show the Faber–Jackson relation for the BCGs and CS1s. Symmetric linear fits to each sample yield

$$L_{\text{BCGs}} \propto \sigma^{5.32 \pm 0.37},$$

$$L_{\text{CS1s}} \propto \sigma^{3.93 \pm 0.21}.$$

We find a slope that is compatible with the standard $L \propto \sigma^4$ relation for non-BCGs and we confirm that σ rises less steeply with luminosity for BCGs.⁷

In the bottom panel of Fig. 16, we investigate how β changes with luminosity. We find that for BCGs, β is approximately constant (within the typical error bars) and has a value ~ 5.5 . For non-BCGs, β varies from values ~ 3 at the low-luminosity end to values

⁷ We find a similar change in slope of the Faber–Jackson relation when using the K -band luminosities of those BCGs with 2MASS photometry and a set of comparison galaxies. This is contrary to recent claims by Batcheldor et al. (2006), who use a much smaller sample of BCGs for their analysis.

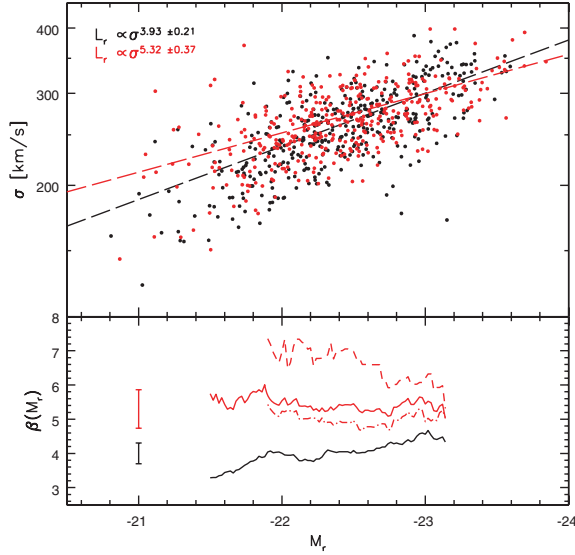


Figure 16. Top panel: the Faber–Jackson relation for BCGs (red) and for the comparison sample CS1s. The dashed lines show the best linear fits to the relations. Bottom panel: the variation of β with M_r , i.e. β determined from galaxies within $M_r \pm 1.0$ for BCGs meeting the early-type criteria (solid red line) and the corresponding CS1s sample (solid black line). The dashed line shows the subset of these BCGs located in clusters with $\sigma_{v,cl} > 400 \text{ km s}^{-1}$, the dash–dotted line the subset of BCGs in clusters with $\sigma_{v,cl} < 500 \text{ km s}^{-1}$. The typical error bars are displayed on the left.

~ 4.5 at high luminosities (a similar range of β , albeit over a larger luminosity interval, was found by Desroches et al. 2007).

Boylan–Kolchin et al. (2006) find that in simulations of dissipationless mergers, β increases with the eccentricity of the merger orbit. They also argue that BCGs are expected to form through anisotropic merging due to the filamentary structure surrounding galaxy clusters.

We test whether β depends on cluster mass by splitting the BCG sample according to cluster velocity dispersion, and fitting β separately for the two samples. We allow the sample to overlap in $\sigma_{v,cl}$ to gain higher statistical significance. We obtain the following results:

$$L_{\text{BCGs}} (\sigma_{v,cl} < 500 \text{ km s}^{-1}) \propto \sigma^{5.22 \pm 0.46},$$

$$L_{\text{BCGs}} (\sigma_{v,cl} > 400 \text{ km s}^{-1}) \propto \sigma^{5.91 \pm 0.69}.$$

The two values of β are just consistent with each other within the errors, and thus we cannot draw strong conclusions. Our results indicate that β is larger for BCGs in more massive clusters. If the scenario put forward by Boylan–Kolchin et al. (2006) is correct, this might imply that the merger orbit eccentricity increases with cluster mass. Another explanation might be that the number of (dissipationless) mergers is larger for BCGs in more massive clusters.

6.3 Stellar populations

The availability of measurements of spectral indices for galaxies in the spectroscopic SDSS catalogue allows us to investigate the stellar populations in BCGs and non-BCGs. Both the distributions of the 4000-Å break (Fig. 11d, measured as $D_n(4000)$; Balogh et al. 1999) and the $H\delta_A$ index (Fig. 11e; Worthey & Ottaviani 1997) demonstrate that the stellar populations of the BCGs and the comparison galaxies are old, as is generally found for galaxies in this mass range (Kauffmann et al. 2003b). The metallicity, measured using the index $[\text{Mg Fe}]'$ (Fig. 11f; Thomas, Maraston & Bender 2003) is also

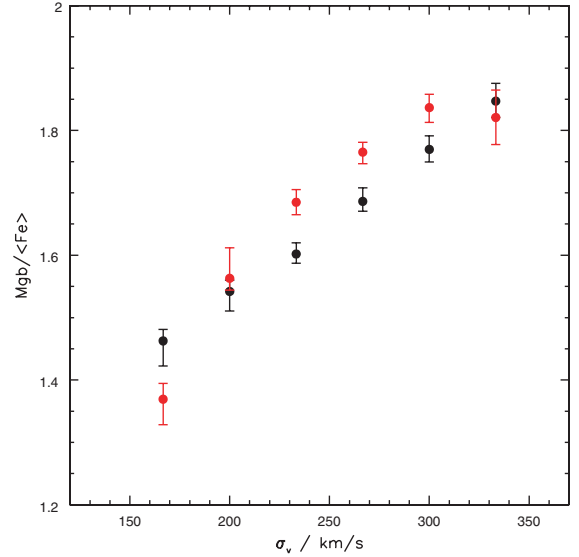


Figure 17. The median value of $\text{Mgb}/\langle \text{Fe} \rangle$ as a function of velocity dispersion for the BCGs (red) and the comparison sample CS1s (black).

typical for giant elliptical galaxies. There is a slight indication that the stellar populations of BCGs are slightly older (larger $D_n(4000)$, lower $H\delta_A$ and higher metallicity), but this is only significant for the $H\delta_A$ index.

It should be noted that these measurements apply only to the galaxy light contained within the fibre, i.e. the inner 3 arcsec, whereas the samples are matched in $g - r$ colour within the 23 mag arcsec $^{-2}$ isophote. In panel (l) of Fig. 10 we find that the colour gradient between the fibre aperture and the iso23 aperture is more prominent in the non-BCGs. This is a confirmation of previous results that colour gradients in BCGs are weak or absent (Garilli et al. 1997), while non-BCG elliptical galaxies are generally redder in the centre (La Barbera et al. 2005). The presence of colour gradients is typically attributed to metallicity gradients (James et al. 2006), however, we do not find evidence for different metallicities in BCGs.

We use the index $\text{Mgb}/\langle \text{Fe} \rangle$ as an indicator of the α/Fe ratio (Thomas et al. 2003) and we find that BCGs have a systematically higher $\text{Mgb}/\langle \text{Fe} \rangle$ value than non-BCGs (Fig. 11g). However, this index is known to correlate strongly with velocity dispersion, so this result is not independent of our previous result that BCGs have systematically larger velocity dispersions. In Fig. 17, we plot $\text{Mgb}/\langle \text{Fe} \rangle$ as a function of velocity dispersion for the BCGs and the comparison sample CS1s. Except in the outermost bins, we do find systematically higher α/Fe ratios in the BCGs. Higher α/Fe ratios can be interpreted as an indication that star formation in the galaxy occurred over a shorter time-scale (Granato et al. 2004). The enhanced radio–AGN activity we find in BCGs (Section 5) may explain why star formation has been shut off on shorter time-scales in the BCGs.

6.4 Emission line properties

We also investigate the strengths of the four emission lines $H\alpha$, $H\beta$, $[\text{O III}]\lambda 5007$ and $[\text{N II}]\lambda 6584$ that are commonly used to classify galaxies according to whether their emission-line luminosity is driven by star formation or AGN activity (Baldwin, Phillips & Terlevich 1981). We limit our sample to galaxies with a signal-to-noise ratio $\text{SNR} > 3$ in the respective line measurement(s). For

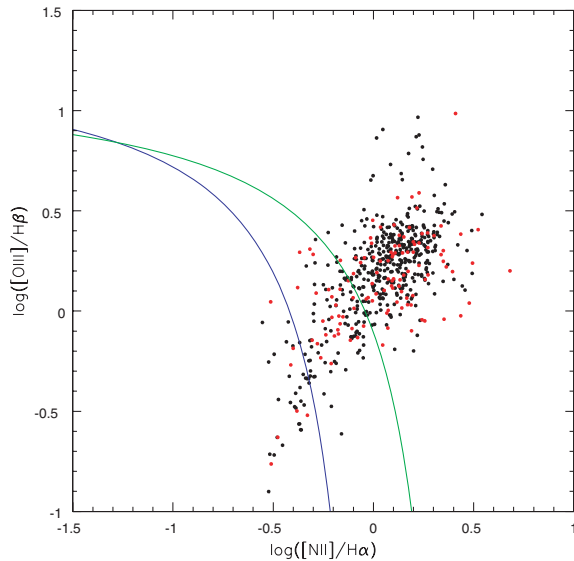


Figure 18. BCGs (red) and the comparison sample CS3s (black) placed into the BPT diagram. Galaxies to the left of the blue line are classified as purely star forming (Kauffmann et al. 2003c), galaxies to the right of the green line as purely AGN (Kewley et al. 2001) and galaxies in between the lines as composite. Only galaxies with SNR > 3 in all four line measurements are shown.

the individual line measurements $H\alpha/H\beta/[O III]/[N II]$, this holds for 56 per cent/42 per cent/64 per cent/50 per cent of the BCGs and 66 per cent/47 per cent/77 per cent/63 per cent of the comparison sample (note that this applies to the CS3s sample). Requiring that SNR > 3 in all four bands simultaneously leaves only 30 per cent of the BCGs and 40 per cent of the comparison sample. These numbers already indicate that the emission lines in BCGs are in general weaker than in non-BCGs, a result which is further confirmed by the distributions of $H\alpha$ and $[O III]$ line luminosities shown in Figs 11(h) and (k). We note that it is particularly the high-mass BCGs in which the emission-line strength is suppressed compared to the comparison sample.

Fig. 18 shows the BPT (Baldwin, Phillips and Terlevich) diagram of BCGs and the comparison sample for those galaxies which satisfy SNR > 3 in all four bands, i.e. 119 (out of 391) BCGs and 472 (out of 1173) non-BCGs. Of these BCGs, seven (i.e. 6 per cent of the line-emitting sample/2 per cent of the complete sample) are classified as star forming, 83 (70 per cent/21 per cent) as AGN and 29 (24 per cent/7 per cent) as composite. Of the non-BCGs, 29 (6 per cent/2 per cent) are star forming, 364 (77 per cent/31 per cent) AGN and 79 (16 per cent/6 per cent) composite. Our sample is too small to draw detailed conclusions from these numbers, except that for both samples, the emission-line flux is dominated by AGN-like emission. Their low $[O III]$ luminosities place the BCGs somewhat lower in the BPT diagram than the non-BCGs, i.e. the BCGs are almost exclusively classified as LINERs, whereas a few galaxies in the comparison sample could be classified as low-luminosity Seyferts.

For case B recombination, the unattenuated value of the Balmer decrement is ~ 3 (more specifically, it is $H\alpha/H\beta = 2.86$ in star-forming galaxies and $H\alpha/H\beta = 3.1$ in AGN; Osterbrock 1989). Remarkably, a considerable fraction of the BCGs in our sample have Balmer decrements below this value (Fig. 11j). It has been noted by Kewley et al. (2006) that 33 per cent of LINERs in the SDSS sample have $H\alpha/H\beta < 2.86$. A possible explanation is that

the fits to the stellar continuum are not entirely reliable for the most massive galaxies, which tend to have very strong metallic absorption lines in their spectra.

6.5 Star formation in BCGs

The results of the previous section suggest that BCGs do not have increased amounts of star formation with respect to the comparison sample. This is somewhat surprising, as there are several BCGs known with signs of recent star formation (blue colours, $H\alpha$ emission; see Crawford et al. 1999), and some cluster cores are known to have extended $H\alpha$ emission structures (e.g. Crawford, Sanders & Fabian 2005). The latter are found to occur exclusively in cooling core clusters (Crawford et al. 1999). However, since the SDSS fibre only probes the inner galaxy, it is insensitive to such surrounding filaments. As for nuclear line emission, Edwards et al. (2007) find that only BCGs at the centres of cooling core clusters are more likely to display emission lines than other massive (cluster) galaxies. They also confirm that in optically selected cluster samples (such as our sample), the BCGs are not more likely to display emission lines than massive comparison galaxies.

Some of the line emission could be attributed to cluster cooling flows instead of optical AGN activity (e.g. Voit & Donahue 1997). In addition, only half of the galaxies have detectable emission lines, so we would prefer a stellar age indicator that can be measured for all galaxies. The strength of the Balmer break $D_n(4000)$ is measurable with a high SNR in all the galaxy spectra and is an indication of the age of the stellar population. Kauffmann et al. (2003a) find that galaxies separate into two distinct populations, with young, star-forming galaxies having $D_n(4000) \lesssim 1.6$. We find that the number of galaxies with $D_n(4000) < 1.6$ is very similar to the number of star-forming galaxies identified from the BPT diagram, for both the BCGs and non-BCGs (see Fig. 19). In Fig. 19, we plot $D_n(4000)$ against $M_u - M_g$ within the iso23 aperture. $M_u - M_g$ also straddles the Balmer break and can thus serve to probe the average stellar

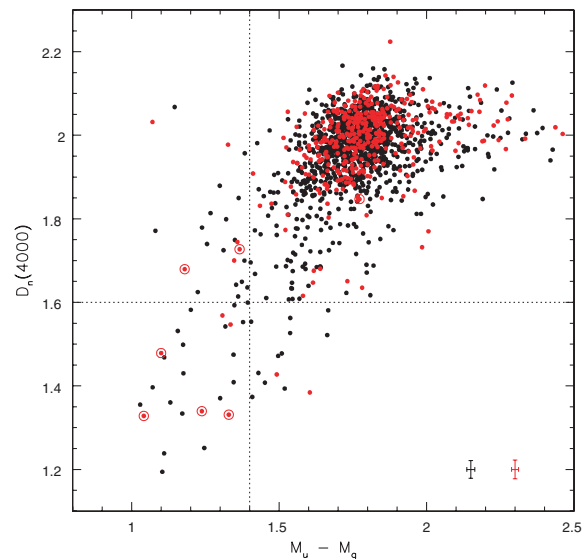


Figure 19. The Balmer break $D_n(4000)$ versus $M_u - M_g$ for the BCGs (red) and the comparison sample CS3s (black). Typical error bars are shown in the lower right-hand corner. The BCGs which were identified as star forming from the BPT diagram are marked by circles. Note that only one of these is an early-type galaxy and is also in the CS1s sample. In the latter sample, there is no BCG and only one comparison galaxy with $D_n(4000) < 1.6$.

population at radii larger than the fibre aperture. The percentage of galaxies with blue $M_u - M_g$ overall colours is compatible for BCGs and non-BCGs, i.e. again there is no indication for enhanced star formation in BCGs. Since we have matched in $M_g - M_r$ colour and have argued that this is essentially a match in stellar mass-to-light ratio, we do not expect a systematic difference in $M_u - M_g$ (and thus this exercise may serve to confirm this argumentation). Without the match in $M_g - M_r$, the comparison sample contains more spiral galaxies, i.e. more star-forming galaxies than the BCG sample.

To conclude, we do not find evidence for increased amounts of star formation in BCGs. However, we would like to caution that our sample is not well suited for such an investigation: we probe only the very centre of the galaxies (and thus cannot detect line emission on larger scales), and we do not have X-ray data for our sample (previous studies suggest there is a strong connection between the cluster X-ray properties and star formation).

7 SUMMARY AND DISCUSSION

We have developed a refined algorithm for selecting BCGs in the C4 cluster catalogue, and we have improved the determination of velocity dispersion and cluster membership. This refined cluster sample consists of 625 galaxy clusters at $z < 0.1$, and spans a wide range in velocity dispersion, from galaxy groups to rich clusters of galaxies. This, along with the detailed information available from SDSS for member galaxies, makes it a suitable local comparison sample for optically selected, high-redshift cluster samples.

Since the original SDSS magnitude measurements of BCGs are affected by excessive sky subtraction, we have developed a procedure to recover more accurate magnitudes by adding a fraction of the difference between the local and global sky background estimates to the radial surface brightness profiles of the SDSS galaxies, and by determining new magnitudes from these corrected profiles. We show that this procedure removes the systematic bias in $z - J$ colour as a function of angular size for elliptical galaxies with photometry from both the SDSS and the 2MASS surveys. We also show that our reconstructed surface brightness profiles of BCGs agree well with previously published aperture photometry, at least to the isophotal limit of $r = 23 \text{ mag arcsec}^{-2}$ within which we measure the flux.

The properties of BCGs are governed by two main factors: their large (stellar) masses and their locations at the bottom of the potential well of their host cluster. Our large sample of BCGs enables us to disentangle the influence of these two factors and to assess the extent to which BCGs differ from ‘ordinary’ massive galaxies.

We investigate the occurrence of radio-loud AGNs in the BCG population and we find that BCGs are more likely to be radio-loud than other galaxies of the same stellar mass. This enhancement ranges from a factor of 10 at stellar masses of $5 \times 10^{10} M_\odot$ to less than a factor of 2 at masses larger than $4 \times 10^{11} M_\odot$. This difference is arguably the most striking difference between BCGs and non-BCGs, and is likely due to the additional hot gas available in groups and clusters to fuel the radio AGN.

The influence of the cluster environment is also evident as an increase in the fraction of dark matter in BCGs. The main observational signature of this excess dark matter is that BCGs have larger radii and higher velocity dispersions than non-BCGs. However, since the conversion of these quantities to dynamical mass depends on the shape of the mass and light profiles of the galaxy, this result could also be mimicked by non-homology between the BCGs and non-BCGs. Either case leads to a different slope of the

Fundamental Plane for BCGs, one that is much closer to the virial plane than the observed Fundamental Plane of normal ellipticals.

It is interesting to note that the differences from ‘normal’ galaxies are particularly evident in lower mass BCGs: these are the galaxies that have a factor of 10 higher probability of being radio-loud and have a significantly larger dark matter mass to light ratio (or a larger degree of non-homology) when compared to the non-BCGs. The low-mass BCGs also deviate most strongly from the generic Fundamental Plane.

We find that the slope of the Faber–Jackson relation is different for BCGs, in that their velocity dispersion rises less steeply for a given increase in luminosity than for non-BCGs. We also find evidence that this effect is stronger for BCGs in massive clusters. Such a change in the Faber–Jackson relation is predicted if these systems form in dissipationless mergers along elliptical orbits. Our results thus support the scenario where BCGs form mainly via dissipationless mergers, and imply that the merger orbits are preferentially radial in the most massive clusters.

A difference in the Faber–Jackson relation also implies that BCGs can follow at most one of the power-law relations often used to estimate the mass of the supermassive black hole at their centre, i.e. either the $M_{\text{BH}} - \sigma_v$ or the $M_{\text{BH}} - L$ relation. In fact, this is already obvious from the parameter distributions shown in Figs 10 and 11: for the same distributions in stellar mass and in luminosity, we find a systematically different distribution in velocity dispersion for our BCGs. The standard relations between black hole mass and bulge velocity dispersion (Tremaine et al. 2002) have likely been derived for non-BCGs and may lead to systematically wrong black hole estimates for the brightest group and cluster galaxies.

We find that BCGs have very similar mean stellar ages and metallicities to non-BCGs. They have slightly higher α/Fe ratios, indicating that their stars may have formed over a shorter time interval. Finally, BCGs display weaker optical emission lines than non-BCGs of the same stellar mass. In both BCGs and non-BCGs, the detected emission lines stem predominantly from low-luminosity optical AGNs. In the accompanying paper (Best et al. 2007), we further investigate the occurrence of AGN activity in BCGs, and argue that the radio-loud and the emission-line AGN activity are independent, unrelated phenomena.

ACKNOWLEDGMENTS

We thank Stefano Zibetti, Anna Gallazzi, Brent Groves, Tim Heckman, Gabriella De Lucia and Mateusz Ruskowski for helpful discussions and comments, and the people behind CAS, particularly Alex Szalay, Ani Thakar and Eric Neilsen for setting up the SkyServer website, whose functionalities eased a large part of this work. We thank the anonymous referee for detailed comments which helped to clarify and strengthen the paper.

PNB would like to thank the Royal Society for generous financial support through its University Research Fellowship scheme.

Funding for the SDSS has been provided by the Alfred P. Sloan Foundation, the Participating Institutions, the National Aeronautics and Space Administration, the National Science Foundation, the US Department of Energy, the Japanese Monbukagakusho and the Max Planck Society. The SDSS website is <http://www.sdss.org/>

The SDSS is managed by the Astrophysical Research Consortium (ARC) for the Participating Institutions. The Participating Institutions are the University of Chicago, Fermilab, the Institute for Advanced Study, the Japan Participation Group, the Johns Hopkins University, the Korean Scientist Group, Los Alamos National Laboratory, the Max-Planck-Institute for Astronomy (MPIA), the

Max-Planck-Institute for Astrophysics (MPA), New Mexico State University, University of Pittsburgh, University of Portsmouth, Princeton University, the United States Naval Observatory and the University of Washington.

REFERENCES

- Allen S. W., Fabian A. C., Edge A. C., Bautz M. W., Furuzawa A., Tawara Y., 1996, *MNRAS*, 283, 263
- Aragon-Salamanca A., Baugh C. M., Kauffmann G., 1998, *MNRAS*, 297, 427
- Baldwin J. A., Phillips M. M., Terlevich R., 1981, *PASP*, 93, 5
- Balogh M. L., Morris S. L., Yee H. K. C., Carlberg R. G., Ellingson E., 1999, *ApJ*, 527, 54
- Batcheldor D., Marconi A., Merritt D., Axon D. J., 2006, *ApJ*, in press (astro-ph/0610264)
- Becker R. H., White R. L., Helfand D. J., 1995, *ApJ*, 450, 559
- Beers T. C., Flynn K., Gebhardt K., 1990, *AJ*, 100, 32
- Bernardi M. et al., 2003a, *AJ*, 125, 1817
- Bernardi M. et al., 2003b, *AJ*, 125, 1849
- Bernardi M. et al., 2003c, *AJ*, 125, 1866
- Bernardi M., Hyde J. B., Sheth R. K., Miller C. J., Nichol R. C., 2007, *AJ*, 133, 1741
- Best P. N., Kauffmann G., Heckman T. M., Ivezić Ž., 2005a, *MNRAS*, 362, 9
- Best P. N., Kauffmann G., Heckman T. M., Brinchmann J., Charlot S., Ivezić Ž., White S. D. M., 2005b, *MNRAS*, 362, 25
- Best P. N., von der Linden A., Kauffmann G., Heckman T. M., Kaiser C. R., 2007, *MNRAS*, in press (doi:10.1111/j.1365-2966.2007.11937.x) (astro-ph/0611197) (this issue)
- Blanton M. R., Roweis S., 2007, *AJ*, 133, 734
- Blanton M. R., Lin H., Lupton R. H., Maley F. M., Young N., Zehavi I., Loveday J., 2003, *AJ*, 125, 2276
- Blanton M. R. et al., 2005, *AJ*, 129, 2562
- Boylan-Kolchin M., Ma C.-P., Quataert E., 2006, *MNRAS*, 369, 1081
- Brinchmann J., Charlot S., White S. D. M., Tremonti C., Kauffmann G., Heckman T., Brinkmann J., 2004, *MNRAS*, 351, 1151
- Brough S., Collins C. A., Burke D. J., Lynam P. D., Mann R. G., 2005, *MNRAS*, 364, 1354
- Burns J. O., 1990, *AJ*, 99, 14
- Condon J. J., Cotton W. D., Greisen E. W., Yin Q. F., Perley R. A., Taylor G. B., Broderick J. J., 1998, *AJ*, 115, 1693
- Crawford C. S., Allen S. W., Ebeling H., Edge A. C., Fabian A. C., 1999, *MNRAS*, 306, 857
- Crawford C. S., Sanders J. S., Fabian A. C., 2005, *MNRAS*, 361, 17
- De Lucia G., Blaizot J., 2007, *MNRAS*, 375, 2
- Desroches L.-B., Quataert E., Ma C.-P., West A. A., 2007, *MNRAS*, 377, 402
- Djorgovski S., Davis M., 1987, *ApJ*, 313, 59
- Dubinski J., 1998, *ApJ*, 502, 141
- Edwards L. O. V., Hudson M. J., Balogh M. L., Smith R. J., 2007, *MNRAS*, in press (doi:10.1111/j.1365-2966.2007.11910.x) arXiv:0704.3242v1)
- Fabian A. C., 1994, *ARA&A*, 32, 277
- Finn R. A. et al., 2005, *ApJ*, 630, 206
- Fukugita M., Shimasaku K., Ichikawa T., 1995, *PASP*, 107, 945
- Garilli B., Sangalli G., Andreon S., Maccagni D., Carrasco L., Recillas E., 1997, *AJ*, 113, 1973
- Gonzalez A. H., Zabludoff A. I., Zaritsky D., 2005, *ApJ*, 618, 195
- Granato G. L., De Zotti G., Silva L., Bressan A., Danese L., 2004, *ApJ*, 600, 580
- Heckman T. M., Kauffmann G., Brinchmann J., Charlot S., Tremonti C., White S. D. M., 2004, *ApJ*, 613, 109
- Hernquist L., 1990, *ApJ*, 356, 359
- Hoessel J. G., Oegerle W. R., Schneider D. P., 1987, *AJ*, 94, 1111
- James P. A., Salaris M., Davies J. I., Philipps S., Cassisi S., 2006, *MNRAS*, 367, 339
- Jarrett T. H., Chester T., Cutri R., Schneider S., Skrutskie M., Huchra J. P., 2000, *AJ*, 119, 2498
- Jørgensen I., Franx M., Kjaergaard P., 1995, *MNRAS*, 276, 1341
- Kauffmann G. et al., 2003a, *MNRAS*, 341, 33
- Kauffmann G. et al., 2003b, *MNRAS*, 341, 54
- Kauffmann G. et al., 2003c, *MNRAS*, 346, 1055
- Kauffmann G., White S. D. M., Heckman T. M., Ménard B., Brinchmann J., Charlot S., Tremonti C., Brinkmann J., 2004, *MNRAS*, 353, 713
- Kewley L. J., Dopita M. A., Sutherland R. S., Heisler C. A., Trevena J., 2001, *ApJ*, 556, 121
- Kewley L. J., Groves B., Kauffmann G., Heckman T., 2006, *MNRAS*, 372, 361
- La Barbera F., de Carvalho R. R., Gal R. R., Busarello G., Merluzzi P., Capaccioli M., Djorgovski S. G., 2005, *ApJ*, 626, L19
- Lauer T. R. et al., 2007, *ApJ*, submitted (astro-ph/0606739)
- Lupton R., Gunn J. E., Ivezić Z., Knapp G. R., Kent S., Yasuda N., 2001, in Harnden F. R., Primini F. A., Payne H. E., eds, *ASP Conf. Ser. Vol. 238, Astronomical Data Analysis Software and Systems X*. Astron. Soc. Pac., San Francisco, p. 269
- Merritt D., 1985, *ApJ*, 289, 18
- Miller C. J. et al., 2005, *AJ*, 130, 968
- Navarro J. F., Frenk C. S., White S. D. M., 1997, *ApJ*, 490, 493
- Oegerle W. R., Hoessel J. G., 1991, *ApJ*, 375, 15
- Osterbrock D. E., 1989, *Astrophysics of Gaseous Nebulae and Active Galactic Nuclei*. University Science Books, Mill Valley, CA
- Ostriker J. P., Tremaine S. D., 1975, *ApJ*, 202, L113
- Padmanabhan N. et al., 2004, *New Astron.*, 9, 329
- Pahre M. A., Djorgovski S. G., de Carvalho R. R., 1998, *AJ*, 116, 1591
- Peterson J. R., Fabian A. C., 2006, *Phys. Rep.*, 427, 1
- Porter A. C., Schneider D. P., Hoessel J. G., 1991, *AJ*, 101, 1561
- Postman M., Lauer T. R., 1995, *ApJ*, 440, 28
- Press W. H., Teukolsky S. A., Vetterling W. T., Flannery B. P., 1992, *Numerical Recipes in C: The Art of Scientific Computing*, 2nd edn. Cambridge Univ. Press, Cambridge
- Ryden B. S., Lauer T. R., Postman M., 1993, *ApJ*, 410, 515
- Sandage A., 1972, *ApJ*, 178, 1
- Schneider D. P., Gunn J. E., Hoessel J. G., 1983, *ApJ*, 264, 337
- Schombert J. M., 1987, *ApJS*, 64, 643
- Silk J., 1976, *ApJ*, 208, 646
- Skrutskie M. F. et al., 2006, *AJ*, 131, 1163
- Springel V. et al., 2005, *Nat*, 435, 629
- Stoughton C. et al., 2002, *AJ*, 123, 485
- Strauss M. A. et al., 2002, *AJ*, 124, 1810
- Thomas D., Maraston C., Bender R., 2003, *MNRAS*, 339, 897
- Thuan T. X., Romanishin W., 1981, *ApJ*, 248, 439
- Tremaine S. et al., 2002, *ApJ*, 574, 740
- Tremonti C. A. et al., 2004, *ApJ*, 613, 898
- Voit G. M., Donahue M., 1997, *ApJ*, 486, 242
- White S. D. M., 1976, *MNRAS*, 174, 19
- White S. D. M. et al., 2005, *A&A*, 444, 365
- Worthey G., Ottaviani D. L., 1997, *ApJS*, 111, 377
- York D. G. et al., 2000, *AJ*, 120, 1579

APPENDIX A: IMPROVING SDSS MAGNITUDES

As described in Section 2.2, we need to correct the photometry of the BCGs and around 200 000 galaxies at $z \lesssim 0.1$ for the fact that the standard SDSS photometric pipeline overestimates the sky background.

The SDSS photometric pipeline PHOTO estimates the global sky within a frame (2048×1498 pixel; 13.5×9.8 arcmin²) from the median value of the pixels in that frame, clipped at 2.3σ . The local sky background is then determined with the same sigma clipping within a box of 256×256 pixel (1.7×1.7 arcmin²) on a grid every 128 pixel, and interpolated between these positions. This sky

estimate is then subtracted from the image, and the photometry is performed on the sky-subtracted image.

If a large fraction of the pixels in a 256×256 pixel box is part of an object rather than blank sky, this procedure causes the local sky to be an overestimate of the true sky background. This may happen for large galaxies, in crowded fields and also around stars, since the wings of the point spread function (PSF) result in a considerable stellar halo.

An overestimation of the sky background results in an underestimation of the surface brightness of the object's pixels – thus, the total effect this has on the flux of an object scales with the square of its radius. This effect is therefore particularly severe for large galaxies. Indeed, Lauer et al. (2007) analyse the photometry of BCGs analysed in Postman & Lauer (1995) that lie in the SDSS DR4 and show that the discrepancy in the estimated luminosity is a function of BCG radius (see also below).

It has been suggested that the true flux of an object may be recovered by using the global sky estimate instead of the local sky estimate (Masataka Fukugita; SDSS mailing list). This approach should allow a new flux measurement without performing a new, independent photometric analysis of the raw images. For each object, the 1D radial surface brightness profile, measured in 15 radial bins, is available. By adding the difference between local sky and global sky to these surface brightnesses, the flux of an object, assuming the global sky level in the respective field, can be measured.

A1 Neighbouring objects

For isolated objects, the above argument implies that the global sky is generally a better sky estimate than the local one. However, for blended objects, we find that the local sky accounts for a large fraction of the flux from the respective neighbours; in these cases, therefore, using the global sky estimates would include flux from the neighbours and thus lead to an overestimate of the luminosity of the object. This is particularly true if the neighbour is a star of similar brightness to the object in question.

We thus need a ‘trigger’ to determine for which objects the local sky should be kept, and for which it should be replaced by the global sky.

We make the trigger for each galaxy i a function of the ratio LR_i of its luminosity L_i to the luminosity L_{nb} of its neighbours (within 1.6 arcmin), defined in the following way:

$$LR_i = -2.5 \log(L_i/L_{nb}),$$

$$L_{nb} = \frac{\sum_{j \in \{\text{galaxies}\}} L_j w_j}{\sum_{j \in \{\text{galaxies}\}} w_j} + 10 \frac{\sum_{j \in \{\text{stars}\}} L_j w_j}{\sum_{j \in \{\text{stars}\}} w_j},$$

$$w_j = e^{-d_{i,j}^2 / (2(2r_{p,i}))^2},$$

where $r_{p,i}$ is the Petrosian radius of the galaxy i , and $d_{i,j}$ is the distance between galaxy i and its neighbour j . Thus, the contribution of a neighbour to L_{nb} is weighted by a Gaussian of width equal to twice the Petrosian radius of the galaxy i – this is the aperture within which the SDSS Petrosian flux is measured. Since we find that the presence of a star close to the object results in a substantial overestimate of the galaxy luminosity if the global sky is used, stars are weighted with an additional factor of 10 (the exact value of this factor makes only little difference, but we do find slightly better results using a factor of 10 rather than 5). We suspect that the stellar halo due to the broad PSF wings is accounted for primarily as local sky background.

We find that for $LR_i < -2.5$, the flux of neighbouring objects is negligible enough for the global sky to be the superior sky estimate. For $LR_i > -1$, the flux of neighbouring objects contributes a substantial fraction of the local sky estimate, so that it cannot be substituted by the global sky.

A2 The method

Rather than simply substituting the global sky for the local sky (or not), we calculate the fraction f_{sky} of the difference between local and global sky to be added to the surface brightness profile of each galaxy according to the following criteria.

- (i) If $\Delta_{sky} = \text{sky}_{local} - \text{sky}_{global} < 0$ in any one of the five bands, then $f_{sky} = 0$. In these cases, the two sky measurements are essentially equivalent, and subtracting flux from the surface brightness profile will add noise to the flux measurement.
- (ii) Values of Δ_{sky} are constrained to be $\leq 10^{-9}$ maggies arcsec $^{-2}$ (‘maggie’ is the linear measure of flux used for the profiles; see Stoughton et al. 2002).
- (iii) The maximum value for f_{sky} is 0.7. In Section A4 we show that this is superior to using $f_{sky}^{max} = 1$. This value is assigned to objects with $LR_i \leq -2.5$.
- (iv) The minimum (non-zero) value for f_{sky}^{min} is 0.1. This value is assigned to objects with $LR_i \geq -1$.
- (v) For objects with $-2.5 < LR_i < -1$, f_{sky} is a linear function of LR_i , being continuous at the endpoints with f_{sky}^{max} and f_{sky}^{min} .

A3 Comparison for the BCGs of Postman & Lauer (1995)

In order to assess the performance of our method to correct the SDSS magnitudes, we need (an) external data set(s) with accurate photometry. We rely on two such data sets: the aperture photometry of BCGs published in Postman & Lauer (1995, referred to as PL95 hereafter), and the 2MASS survey (Skrutskie et al. 2006). The method is considered successful if it can simultaneously reproduce the curve-of-growth of a large fraction of the PL95 BCGs, and if galaxies do not show any systematic bias in their median SDSS–2MASS colours.

In Fig. A1 we demonstrate that our method can reproduce the aperture photometry of the PL95 BCG sample. Of the 119 BCGs in that sample, 35 have imaging data from DR5, and 12 are also in our BCG sample (which was based on DR3). We show the curve-of-growth of six representative BCGs in Fig. A1. We assume $r' - R_c = 0.25$ as the typical colour of an elliptical at $z = 0$ (Fukugita, Shimasaku & Ichikawa 1995) in order to compare measurements taken in different bands.

The examples show how the original SDSS photometry breaks down at radii larger than ~ 20 arcsec. Our improved photometry is able to reproduce the PL95 aperture photometry much better, out to $\gtrsim 80$ arcsec. Of the 12 BCGs in common with our sample, our photometry fails to accurately reproduce PL95 only for the BCG of Abell 160 (C4_DR3_2025): this is because PHOTO attributes a large fraction of the BCG luminosity to a secondary nucleus; hence LR is rather large, and only little sky background is added to the brightness profile. Of the 35 BCGs in DR5, this is also the case for the BCG of Abell 1185 (not shown). The crowding in the fields around the BCGs of Abell 2040 and 2052 also leads to an underestimation of the flux by about 0.2 mag (not shown).

In addition to bad sky subtraction, noise in the surface brightness profile plays an important role particularly at large radii, as can be seen in the curve-of-growth of the BCG of Abell 779 (Fig. A1). The

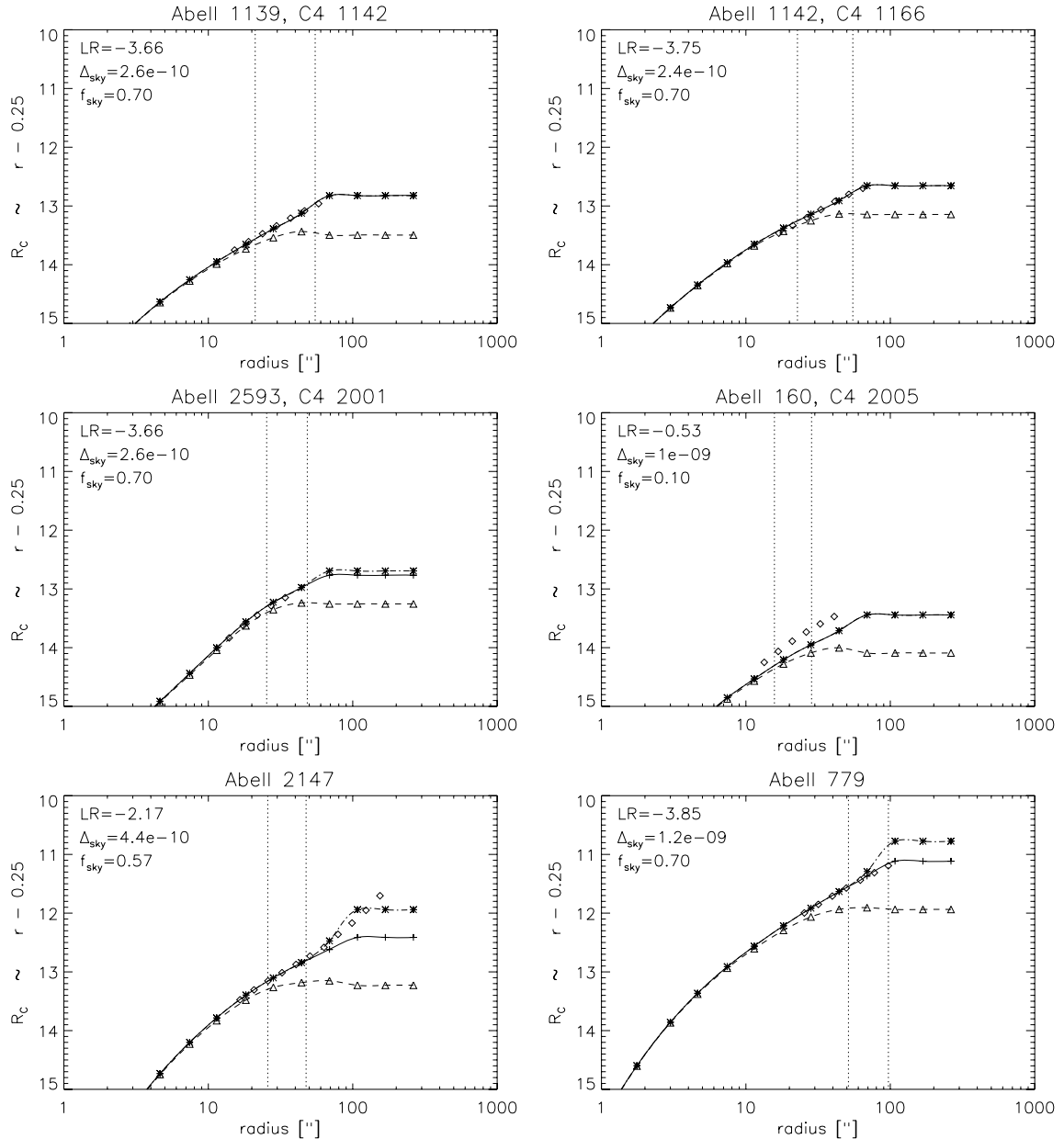


Figure A1. Comparison of the aperture photometry of Postman & Lauer (1995) (shown as diamonds) and SDSS photometry for six BCGs. The uncorrected SDSS magnitudes are shown as triangles, with the respective cubic spline fit as a dashed line. By adding flux of $f_{\text{sky}} \Delta_{\text{sky}}$, we obtain the curve-of-growth shown by \times symbols and as dash-dotted line. Noisy photometry at large radii can cause jumps in the curve-of-growth; this can be alleviated by the method described in the text, and is shown as \times symbols, and as solid line. The dotted lines indicate the radii at which the surface brightness profile reaches a magnitude of $r = 23 \text{ mag arcsec}^{-2}$ (left line) and $r = 24 \text{ mag arcsec}^{-2}$ (right line).

last non-zero bin of the SDSS surface brightness profile causes a jump in total magnitude of more than 0.5 mag, which is not seen in the PL95 photometry. To avoid such jumps, we compare the cumulative flux for each bin of radius $\geq 18 \text{ arcsec}$ to the flux predicted for that bin from the slope of the curve-of-growth from the two bins prior in radius. If the flux is more than 30 per cent larger than predicted (or if the surface brightness in the respective bin is negative), the measured flux is substituted by the predicted flux. For several BCGs this procedure improves the agreement between the SDSS and PL95 brightness profiles. For one (the BCG of Abell 2147), this causes disagreement at large radii. However, this occurs at a significantly larger radius than the one within which we measure the magnitudes.

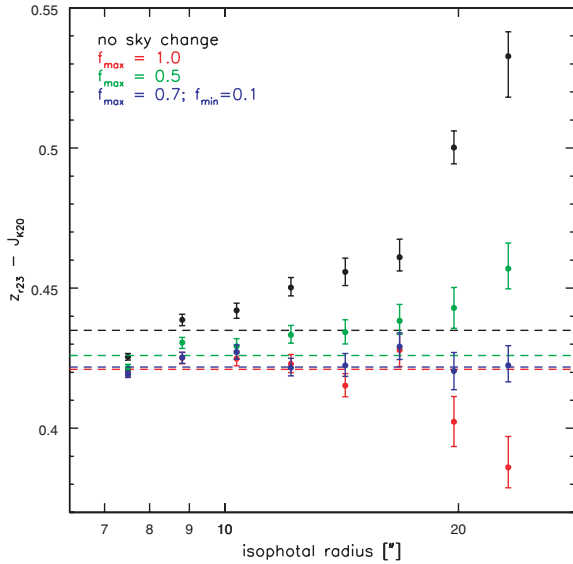
A4 Comparison to 2MASS magnitudes

Of the 200 000 unique SDSS galaxies at $z < 0.1$, about half have a counterpart in the 2MASS survey's Extended Source Catalog (XSC); we made use of the list of 2MASS objects matched to SDSS galaxies provided via the NYU VAGC (Blanton et al. 2005) to identify these galaxies and obtain their 2MASS properties.

In order to be able to directly compare the SDSS and XSC data, we work with isophotal magnitudes. One of the magnitude measurements provided by 2MASS is measured within the $K = 20 \text{ mag arcsec}^{-2}$ isophote. $K = 20$ corresponds approximately to $r = 23$, hence we measure SDSS magnitudes within the radius where the surface brightness profile drops to $r = 23 \text{ mag arcsec}^{-2}$.

Table A1. Comparison of the results of Kolmogorov–Smirnov tests (expressed as the decimal logarithm of 1 minus the confidence level at which the null hypothesis, that the distributions are drawn from an identical parent population, can be rejected) on BCG and non-BCG distributions of various parameters, for different versions of sky subtraction applied to the SDSS photometry.

Sky subtraction	R_{50}	$R_{\text{iso}23}$	c'	μ_{50}	$\mu_{\text{iso}23}$	b/a	$\Delta(g-r)$	σ_v	$M_{\text{dyn},50}/M_*$	$D_n(4000)$	$H\delta_A$	$L(H\alpha)$	$L(H\beta)$
$f_{\text{sky}}^{\text{max}} = 0.7$	-5.44	-3.60	-4.58	-8.78	-12.43	-7.28	-3.13	-2.06	-13.33	-0.88	-2.67	-1.60	-0.01
$f_{\text{sky}}^{\text{max}} = 0.5$	-6.13	-3.37	-4.84	-10.38	-14.46	-7.71	-2.61	-2.27	-14.00	-0.57	-2.71	-1.04	-0.04
$f_{\text{sky}}^{\text{max}} = 1.0$	-4.91	-3.29	-3.48	-6.44	-12.76	-6.44	-2.16	-2.19	-12.57	-0.61	-2.74	-1.75	-0.01

**Figure A2.** The difference between SDSS z magnitude (measured within the $r = 23$ mag arcsec $^{-2}$ radius) and 2MASS J magnitude (measured within the $K = 20$ mag arcsec $^{-2}$ radius) as a function of galaxy size (given by the $r = 23$ mag arcsec $^{-2}$ isophotal radius). We measure the median difference in bins of radius; the error bars denote the 68 per cent levels of the distribution in each bin, divided by the square root of the number of galaxies in that bin. For the black symbols, the sky subtraction has not been changed from the original SDSS value. For the red symbols, $f_{\text{sky}}^{\text{max}} = 1.0$, i.e. if an object meets the criteria to replace the local by the global sky, the full difference is added (see Section A2 for details). For the green symbols, $f_{\text{sky}}^{\text{max}} = 0.5$, and for the blue symbols, $f_{\text{sky}}^{\text{max}} = 0.7$ and $f_{\text{sky}}^{\text{min}} = 0.1$. The dashed lines show the median values for all galaxies.

We compare these magnitudes for elliptical galaxies, selected using standard cuts that have been used in previous SDSS studies (i.e. $c_{\text{SDSS}} = R_{90}^{\text{SDSS}}/R_{50}^{\text{SDSS}} > 2.86$ and $g_{\text{petro}}^{\text{SDSS}} - r_{\text{petro}}^{\text{SDSS}}$). We also limit the sample to galaxies where the SDSS and 2MASS radii agree to within 30 per cent (this criterion changes for each magnitude measurement). We consider only galaxies with a radius larger than 7 arcsec, the minimum radius necessary to avoid PSF effects for 2MASS data (Jarrett et al. 2000). After correcting for galactic extinction (and converting the J -band magnitude to an AB magnitude), we compare the SDSS z -band magnitudes to the 2MASS J -band magnitudes, since these bands are adjacent in wavelength and thus colour differences from different stellar populations can be expected to be minimal.

In Fig. A2, we investigate the colour ($z_{23} - J_{K20}$) as a function of galaxy size (given by the $r = 23$ mag arcsec $^{-2}$ isophotal radius in the SDSS) for four different sky subtractions. Clearly, for the original SDSS sky subtraction, the colour term is a strong function of galaxy size, indicating that the sky is systematically oversubtracted in the optical band. This accounts for a systematic difference of the

order of 0.1 mag for galaxies larger than 20 arcsec (for individual galaxies, this may be much more, as demonstrated by Lauer et al. 2007). However, substituting the local sky estimate by the global one (i.e. $f_{\text{sky}}^{\text{max}} = 1.0$) leads to an underestimation of the sky, and thus an overestimation of the luminosity. We find that with $f_{\text{sky}}^{\text{max}} = 0.7$, there is little variation of the median colour term with galaxy size, and no systematic trend (note that setting $f_{\text{sky}}^{\text{min}} = 0.1$ makes only a small difference).

A5 Final magnitudes

The isophotal magnitudes are not redshift independent because of cosmological surface brightness dimming. We thus modify the algorithm to correct both for $(1+z)^4$ surface brightness dimming and for galactic extinction (i.e. these corrections applied directly to the radial profile before the magnitudes are measured).

We choose to use isophotal magnitudes corresponding to $r = 23$ at $z = 0$ (i.e. $r = 23.41$ at $z = 0.1$). This is a rather bright cut-off, but is less sensitive to residual errors in the sky subtraction and/or surface brightness measurements (cf. Fig. A1).

A6 Influence of the sky subtraction on our results

Our analysis of BCG properties (Section 6) as a function of stellar mass depends critically on the correct determination of the luminosities of the objects in our sample. If the luminosities we assign to BCGs are underestimated, then the comparison galaxies (which are matched in stellar mass) would be systematically less massive than the BCG, leading to possibly spurious differences in their physical properties.

To estimate the effect that sky subtraction has on our results, we repeat the analysis presented in Section 6 with photometry derived with values of $f_{\text{sky}}^{\text{max}} = 0.5$ and 1.0. To evaluate whether there could be significant quantitative effects on our results, we compare the results of the Kolmogorov–Smirnov test on the BCG and non-BCG distributions for several parameters (as shown also in Figs 10 and 11) in Table A1. We find only minor differences to our initial results; none of our conclusions is altered as a result of using a different value of $f_{\text{sky}}^{\text{max}}$.

APPENDIX B: CLUSTER EXAMPLES

In the following we present finding charts and redshift histograms for clusters referred to in the text (Figs B1–B4). The finding charts are centred on the BCG, and spectroscopically confirmed cluster members are marked by triangles. In the redshift histograms, a short-dashed line indicates the cluster redshift, the long-dashed line the redshift of the BCG and the dotted lines the $\pm 3\sigma_{v,cl}$ limits. Furthermore, the redshift (both the C4 and our measurement) as well as the velocity dispersion measurements (given in km s $^{-1}$) are listed in the redshift histograms.

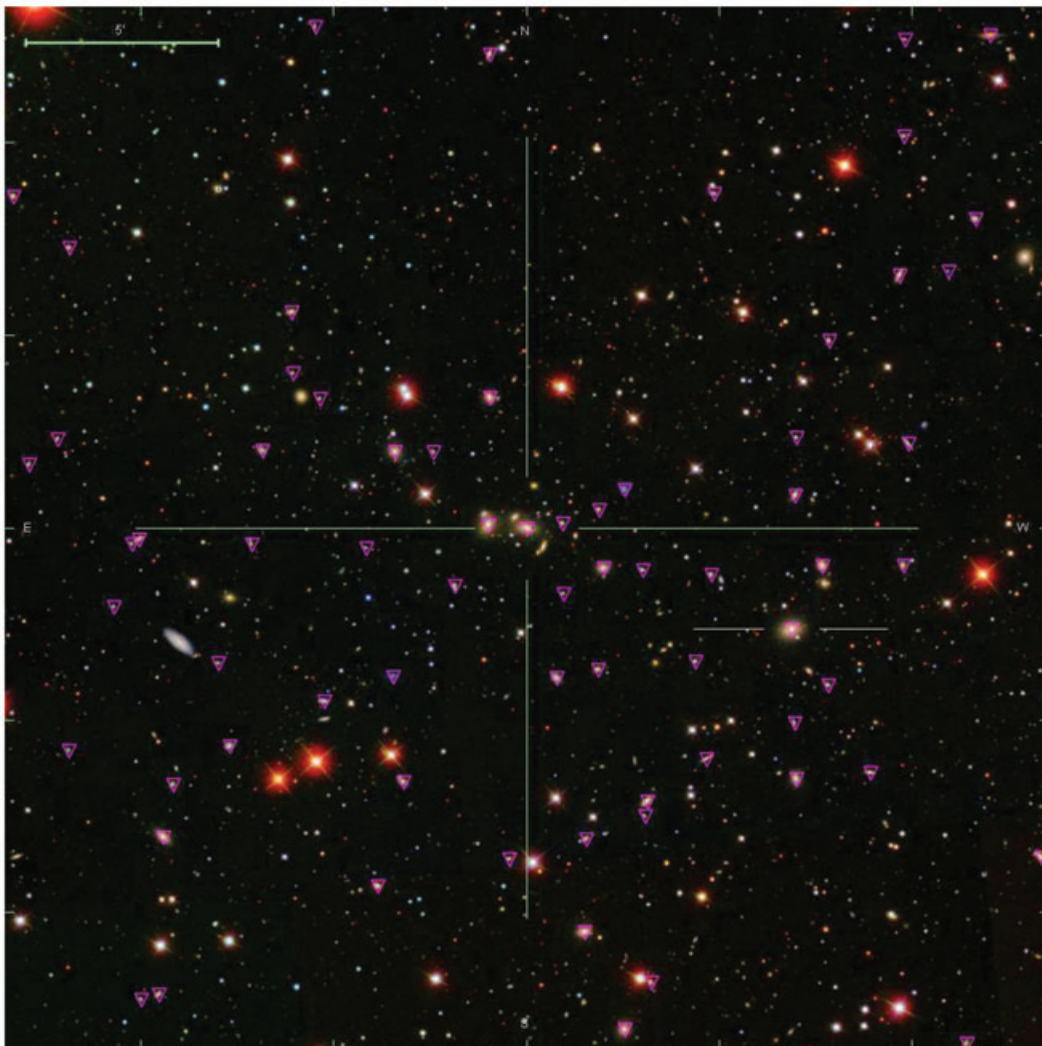
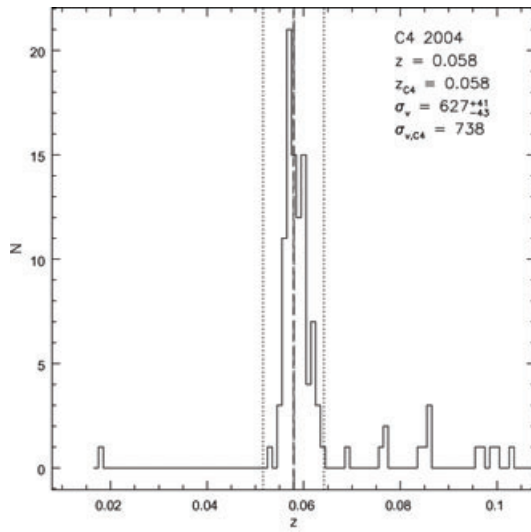


Figure B1. C4_2003: since most galaxies seem to cluster around the galaxy shown at the centre of this image, this is the galaxy we identify as the BCG, even though the galaxy about 6 arcmin west-south-west of the centre (marked by two lines) is brighter by a third of a magnitude. The R_{200} of this cluster is 1.5 Mpc, which translates to ~ 20 arcmin.

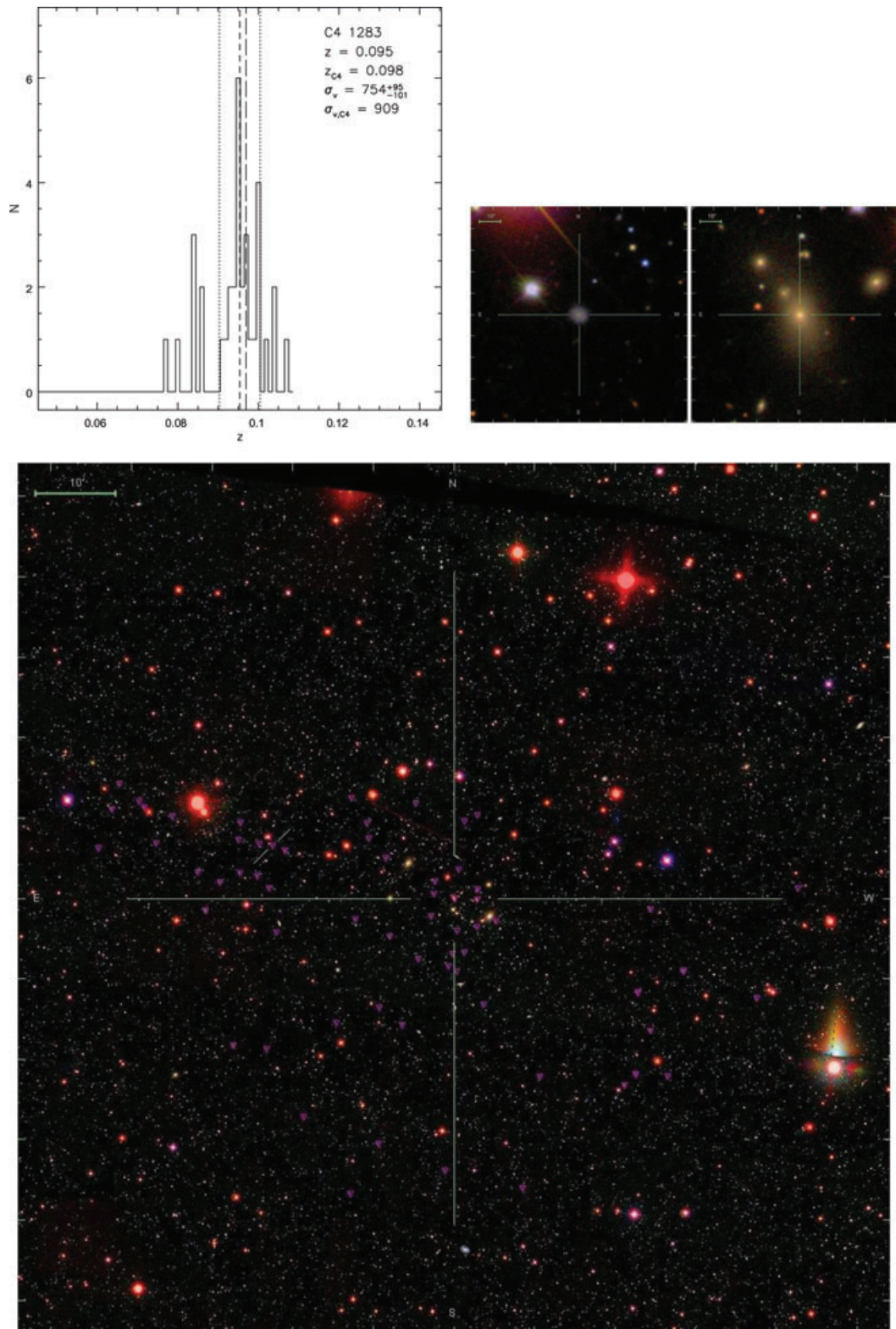


Figure B2. C4_DR3_1283: for this cluster, the C4 mean galaxy (marked by diagonal lines in the finding chart) lies 2.8 Mpc from the BCG which we identify. The large-scale distribution of galaxies at the cluster redshift suggests that C4 selected part of the infall region of this cluster, but fails to pick up the cluster itself. Note that the brightest galaxy in the field is IC 0504 at $z = 0.013$, whereas many of the other bright galaxies in the foreground belong to C4_DR3_1356 at $z = 0.03$. Above, we show thumbnail images of the C4 mean galaxy (left) and our BCG (right).

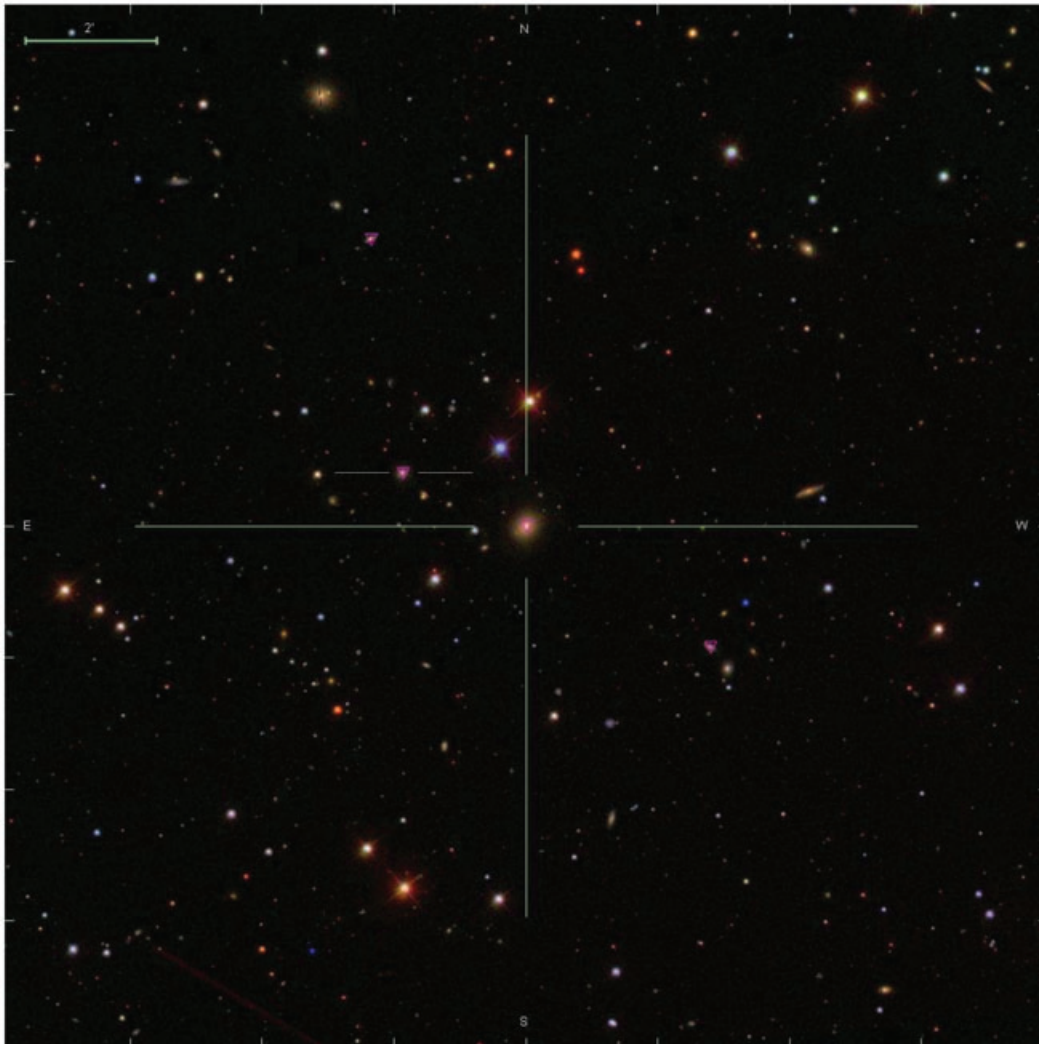
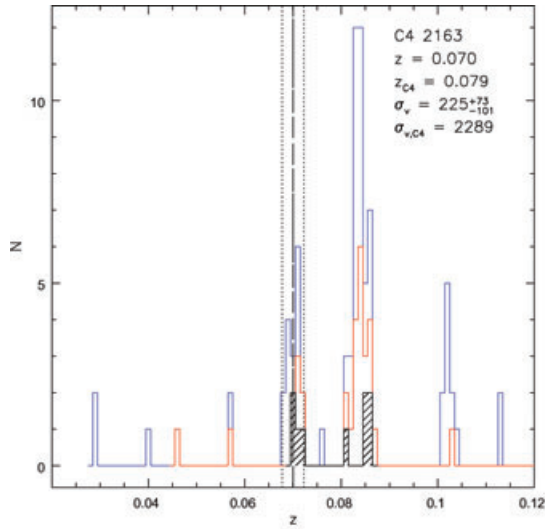


Figure B3. C4_DR3_2163: in the C4 catalogue, this cluster is listed as a structure at $z = 0.079$, with $\sigma_{v,cl} > 2000 \text{ km s}^{-1}$. The mean galaxy is marked in the finding chart above and is part of the group of galaxies at $z = 0.07$, which our algorithm identifies. In the redshift histogram, we show the distribution of galaxies within projections of $1R_{200}$ (black, shaded), $3R_{200}$ (red) and $5R_{200}$ (blue). Obviously, the difference in the redshift measurements as well as the large C4 velocity dispersion are due to another structure at $z \sim 0.082$. In Fig. B4, we show that this background structure is associated with C4_2124.

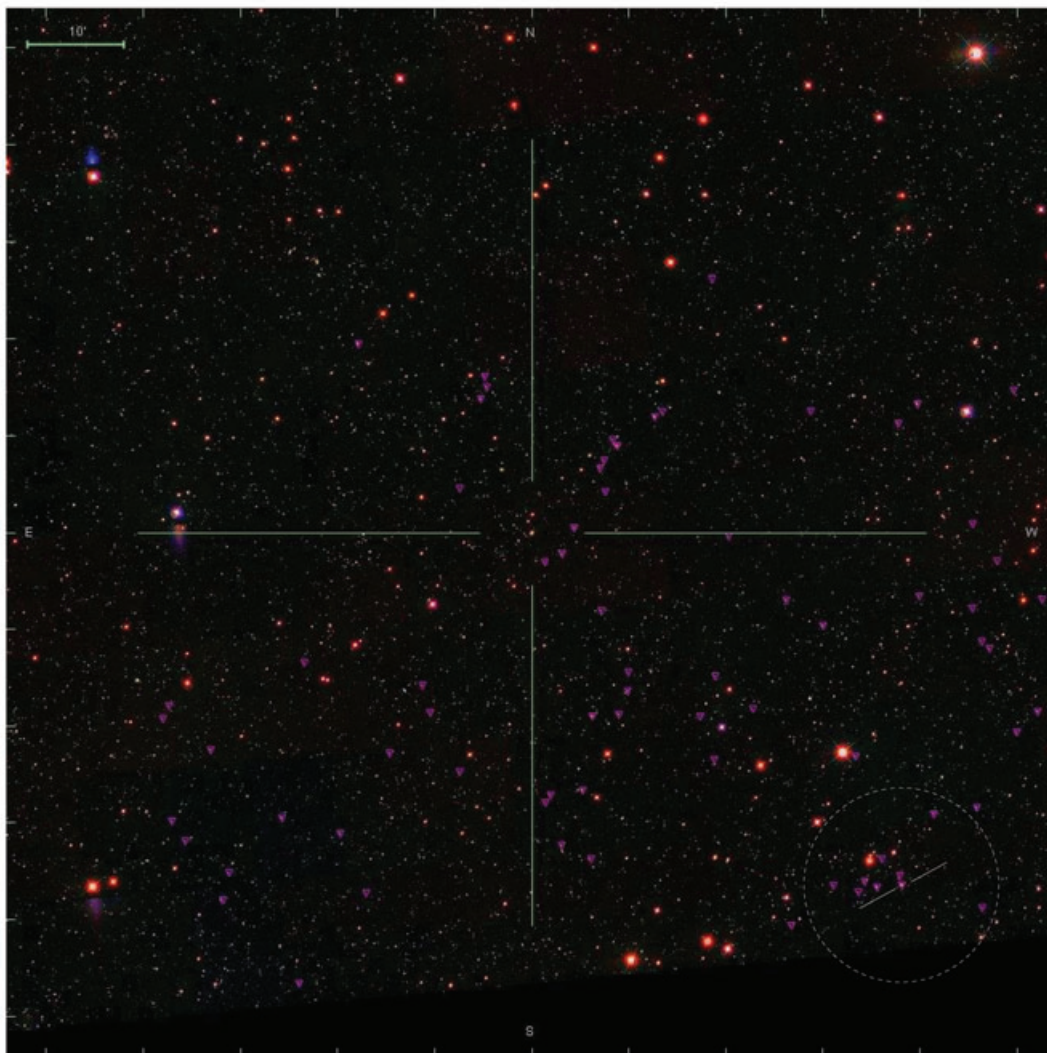
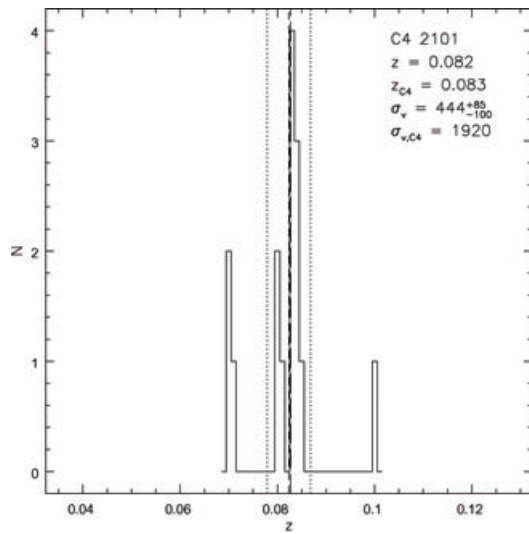


Figure B4. C4_2124: the finding chart below is not centred on the BCG of C4_2124, but on the BCG of C4_DR3_2163, in order to illustrate the sheet-like structure at $z \sim 0.082$ which led to the deviating redshift measurement for C4_DR3_2163. The BCG of C4_2124 is marked in the finding chart, and its R_{200} (equivalent to 1 Mpc) is indicated by a dashed circle.

SUPPLEMENTARY MATERIAL

The following supplementary material is available for this article.

Table 1. Our catalogue of BCGs for the C4 cluster catalogue, along with the cluster properties derived by our algorithm. Note that columns (1) and (2) refer to the C4 cluster ID (see footnote in Section 3.1); column (7) gives the number of galaxies from which the cluster redshift and velocity dispersion were determined.

This material is available as part of the online article from: <http://www.blackwell-synergy.com/doi/abs/10.1111/j.1365-2966.2007.11940.x> (this link will take you to the article abstract).

Please note: Blackwell Publishing is not responsible for the content or functionality of any supplementary materials supplied by the authors. Any queries (other than missing material) should be directed to the corresponding author for the article.

This paper has been typeset from a \TeX/L\TeX file prepared by the author.